# Performance of Machine Learning for Ozone Modeling in Southern California during the COVID-19 Shutdown

Khanh Do[1,2], Arash Kashfi Yeganeh[1,2], Ziqi Gao[3], Cesunica E. Ivey[1,2,4*]

*Corresponding Author: iveyc@berkeley.edu

[1]Department of Chemical and Environmental Engineering, University of California Riverside, Riverside, CA, USA

[2]Center for Environmental Research and Technology, Riverside, CA, USA

[3]Department of Civil and Environmental Engineering, Georgia Institute of Technology, Atlanta, GA, USA

[4]Now at Department of Civil and Environmental Engineering, University of California, Berkeley, Berkeley, CA, USA

This manuscript is a non-peer reviewed preprint submitted to *EarthArXiv* and is currently undergoing peer review.

## Abstract

We combine machine learning (ML) and geospatial interpolations to create two-dimensional high-resolution ozone concentration fields over the South Coast Air Basin (SoCAB) for the entire year of 2020. Three spatial interpolation methods (bicubic, IDW, and ordinary kriging) were employed. The predicted ozone concentration fields were constructed using 15 building sites predicted by the ML method, and random forest regression was employed to test the predictability of 2020 data based on input data from past years. Spatially interpolated ozone concentrations were evaluated at twelve sites that were independent of the actual spatial interpolations to find the most suitable method for SoCAB. Ordinary kriging interpolation had the best performance overall for 2020: concentrations were overestimated for Anaheim, Compton, LA North Main Street, LAX, Rubidoux, and San Gabriel sites and underestimated for Banning, Glendora, Lake Elsinore, and Mira Loma sites. The model performance improved from the West to the East, exhibiting better predictions for inland sites. The model is best at interpolating ozone concentrations inside the sampling region (bounded by the building sites), with $R^2$ ranging from 0.56 to 0.85 for those sites, as prediction deficiencies occurred at the periphery of the sampling region, with the lowest $R^2$ of 0.39 for Winchester. All interpolation methods poorly predicted and underestimated ozone concentrations in Crestline during summer (up to 19 ppb). Poor performance for Crestline indicates that the site has a distribution of air pollution level independent from all other sites. Therefore, historical data from coastal and inland sites should not be used to predict ozone in Crestline using data-driven spatial interpolation approaches. The study demonstrates the utility of ML and geospatial techniques for evaluating air pollution levels during anomalous periods. Both ML and CMAQ do not fully capture the irregularities caused by emission reductions during the COVID-19 lockdown period (March – May) in the SoCAB. The results from ML indicate that there has never been a similar pattern in air quality to that of the COVID-19 lockdown in the past. Including 2020 training data in the ML model training improves the model's performance and its ability to predict future abnormalities in air quality.

## Keywords

Ozone, machine learning, COVID-19, modeling, Southern California

## 1. Introduction

In the atmosphere, the non-linear relationship between nitrogen oxides ($NO_X$), volatile organic compounds (VOCs), and ozone is complex. In the United States, the COVID-19 pandemic and the ensuing shutdown presented an unintentionally optimal period to observe, revise, and improve our existing air quality models and observe the sensitivity of the $NO_X$-VOC-ozone relationship in real time. In California, the pandemic shutdown began on March 16, 2020, where significantly reduced traffic volume was observed. In Los Angeles and Ventura Counties, there was approximately a 30% decrease in vehicle miles traveled (VMT) on weekdays and up to a 40% decrease on weekends in 2020 (Caltrans, 2023). This unusual event temporarily changed the conventional distribution of primary and secondary air pollutants in the South Coast Air Basin (SoCAB). NOx and VOC emissions declined with the reduction in traffic flow (Jiang et al., 2021). As a result, we expected a drop in ozone concentrations in Southern California. Several studies were published regarding the pandemic that investigated the effects of the COVID-19 shutdown on air pollutants. Jiang et al., used WRF-Chem to simulate the major air pollutants under two scenarios (i.e., before lockdown and during lockdown) and found an increase in ozone in urban areas due to emission reduction during the lockdown (Jiang et al., 2021). The COVID-19 shutdown provided an estimation of the impacts of future large-scale emission reduction strategies on ozone formation in SoCAB (Ivey et al., 2020).

Over the past several decades, ozone levels in Southern California significantly decreased as a result of emissions control programs implemented by the South Coast Air Quality Management District (SCAQMD), thereby reducing emissions from mobile sources and shifting to renewable energy sources (Lurmann et al., 2015; South Coast Air Quality Management District, 2017). However, during the past decade, ozone concentrations in the SoCAB have slightly plateaued despite further emissions reductions (Figure 1) (Do et al., 2023).

This paper focuses on the performance of deterministic and statistical models under rapid changes in emissions and meteorological conditions. Furthermore, we aim to answer the question of whether there were other periods with emissions changes similar to the COVID-19 lockdown period within the past few decades. Chemical transport models (CTM) are conventionally used for air quality research and regulatory purposes. The Community Multiscale Air Quality (CMAQ) modeling system, developed by the U.S. Environmental Protection Agency (EPA), is well-known for multi-day air quality simulations to estimate air pollutant concentrations with prescribed emissions and meteorology inputs (Ooka et al., 2011; Rao et al., 1996; D. C. Wong et al., 2012). From the model outputs, scientists and regulators can better predict the interactions between future emissions, meteorology, and air pollutants to strengthen recommendations for emissions control programs. Zhu et al. used CMAQ to investigate the sensitivity of ozone and particulate matter less than 2.5 microns ($PM_{2.5}$) to incremental changes in volatile organic compounds (VOC) by updating the VOC emissions from recent literature, and simulated maximum daily 8-hour ozone concentrations increased by 17.4 ppb and 15.6 ppb in summer and winter, respectively (Zhu et al., 2019). With a similar approach, Karamchandani et al., found that near-recent regulatory modeling for SoCAB generally underestimated the response of ozone design values to the changes in precursor emissions (Karamchandani et al., 2017).

Recently, ML as an alternative modeling approach has attracted more attention from air quality researchers. Although ML and chemical transport models have a similar goal to accurately predict air pollution, ML heavily depends on the quality and quantity of data available. Conversely, CTMs are based on first principles equations and are initiated with interpolated observation data, hence avoiding most obstacles introduced by data missingness in observations. In contrast with CTMs, which produce larger-scale, spatially resolved outputs, ML only provides predictions strictly at trained locations when used for ambient air quality applications. SCAQMD operates 38 air monitoring stations in Southern California over an area of approximately 10,743 square miles, including SoCAB, portions of the Salton Sea Air Basin, and Mojave Desert Air Basin, with an average of 283 square miles per monitoring station (Miyasato et al., 2016; South Coast Air Quality Management District, 2017). Due to the relative sparseness of monitoring stations and locality of air pollutants, using air monitoring stations to represent spatially-varying air quality over a large area may result in incorrect information (Apte et al., 2017). To overcome this limitation when high-resolution measurements are not available, researchers opt to use spatial interpolation methods (e.g., nearest neighbors, linear or polynomial interpolation, continuous natural neighbor interpolation, etc.) (Joseph et al., 2013). Yu et al., evaluated 14 unique spatial modeling methods for eight air pollutants in Atlanta, Georgia for developing spatiotemporal air pollutant concentrations fields (Yu et al., 2018). Wong et al., assessed four spatial interpolation methods (spatial averaging, nearest neighbor, inverse distance weighting (IDW), and kriging) to estimate ozone and $PM_{10}$ air concentrations (Wong et al., 2004). In this paper, we compare three spatial interpolation techniques to the CMAQ model and evaluate biases related to COVID-19 lockdown anomalies.

# 2. Study Area and Datasets

This study targeted the Southern California region, including Los Angeles, Orange County, Riverside, and San Bernardino counties. The region has been historically challenged with poor air quality, with especially higher ozone concentrations than the rest of the United States. The coastal areas tend to have higher relative humidity (RH) and lower temperatures than inland Southern California. Since the turn of the century, SoCAB has been designated as a nonattainment area for the 1997 8-hour ozone standard (80 ppb), with design values for ozone well above the 2015 standard of 70 ppb (Figure 1). In 2019, the maximum daily 8-hour average (MDA8) ozone concentration in SoCAB was 108 ppb at the design value location with a classification of “extreme” (Redlands, California) (California Air Resources Board, 2023).

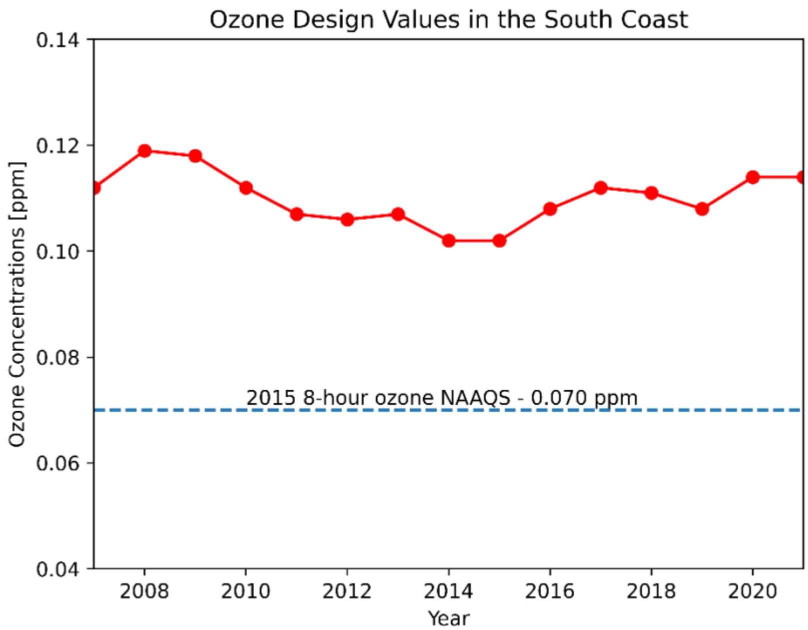


*Figure 1. Ozone design values for the South Coast Air Basin from 2006 to 2020 ([https://www.epa.gov/air-trends/air-quality-design-values](https://www.epa.gov/air-trends/air-quality-design-values)).*

## 2.1 Model Input Data

The input meteorological data for the CMAQ simulation were generated using the Weather Research and Forecasting (WRF) model. WRF was initiated using initial and boundary condition meteorology data from the North American Mesoscale (NAM) Forecast System integrated with high-resolution sea surface temperature (SST) from the Group for High Resolution Sea Surface Temperature. We used the WRF Objective Analysis program to improve the meteorological simulation, and this step blends observed surface and upper air observations with background WRF fields. The surface and upper air observations are sourced from NCEP ADP Global Surface Observational Weather Data (ds461) and NCEP ADP Global Upper Air Observational Weather Data (ds351) via the National Center for Atmospheric Research's Research Data Archive, respectively (Wang et al., 2017).

We re-projected gridded 4 km emissions from 2019 for the year 2020 using a two-step adjustment to account for changes due to the COVID-19 (Zhu et al., 2023). In the first step, a linear projection factor

(Eq. 1) was applied to 2019 gridded emissions based on SCAQMD basin-wide, total annual emissions spanning from 2012 to 2034, where the District's future projections began in the year 2020. The correction factor was calculated for seven air pollutant groups (total organic gases, reactive organic gases, CO, $NO_X$, $SO_X$, $NH_3$, PM).

$$Linear\ projection\ factor = \frac{2020\ emis - 2019\ emis}{2019\ emis} \quad (1)$$

The second step accounted for traffic reductions due to the COVID-19 lockdown, and reductions were highest from March to May 2020 then slowly but not fully rebounding to pre-lockdown levels toward the end of 2020 (Caltrans, 2023). SCAQMD basin-wide projections understandably did not reflect the decrease in mobile source emissions due to traffic reductions. Moreover, weekly traffic metrics in 2020 were acquired for the total flow, flow change, and speed change at 2991 locations in Southern California (Tanvir et al., 2023). Since the traffic data were not evenly distributed over the study domain, we used k-nearest neighbors (k-NN) to obtain the traffic data for grid cells (locations) that had no more than five reported data points (k value ≤ 5). For the grid cells with more than five reported data points, we normalized traffic volume and then averaged the normalized data.

## 2.2 Machine Learning Inputs

We used two air quality features (i.e., $NO_2$ and NO) and four meteorological features (i.e., temperature, relative humidity, wind speed, and wind direction) from 15 air monitoring sites in SoCAB (Figure 2). Hourly meteorological and air quality data used for ML training and validation were obtained from the Air Quality System (AQS) data mart (https://aqs.epa.gov/aqsweb/airdata/download_files.html#Raw, last access Jan. 19, 2023). We checked the data to ensure the hourly data was available for all training features. If there was a missing data point for one of the features, we removed the invalid hour and all corresponding features. The date range of the model training data was 2009-2010 and 2016-2019 for all 15 sites (Figure 2). The period from 2011-2015 was not included in our models due to the limited availability of wind direction and wind speed at the sites. We used 2020 data for model testing and evaluation (

Table 1).

*Table 1. Data summary for machine learning modeling.*

| | |
|---|---|
| **Ground Monitoring Locations** | Anaheim, Azusa, Banning, Compton, Fontana, Glendora, Lake Elsinore, LAX, LA North Main Street, Mira Loma, Rubidoux, San Gabriel, Santa Clarita, San Bernardino, Upland |
| **Features** | $NO_2$, NO, temperature, relative humidity, wind speed, wind direction |
| **Label** | Ozone |
| **Data sources** | EPA AQS data mart, CARB AQMIS |
| **Training years** | 2009, 2010, 2016, 2017, 2018, 2019 |
| **Evaluation year** | 2020 |

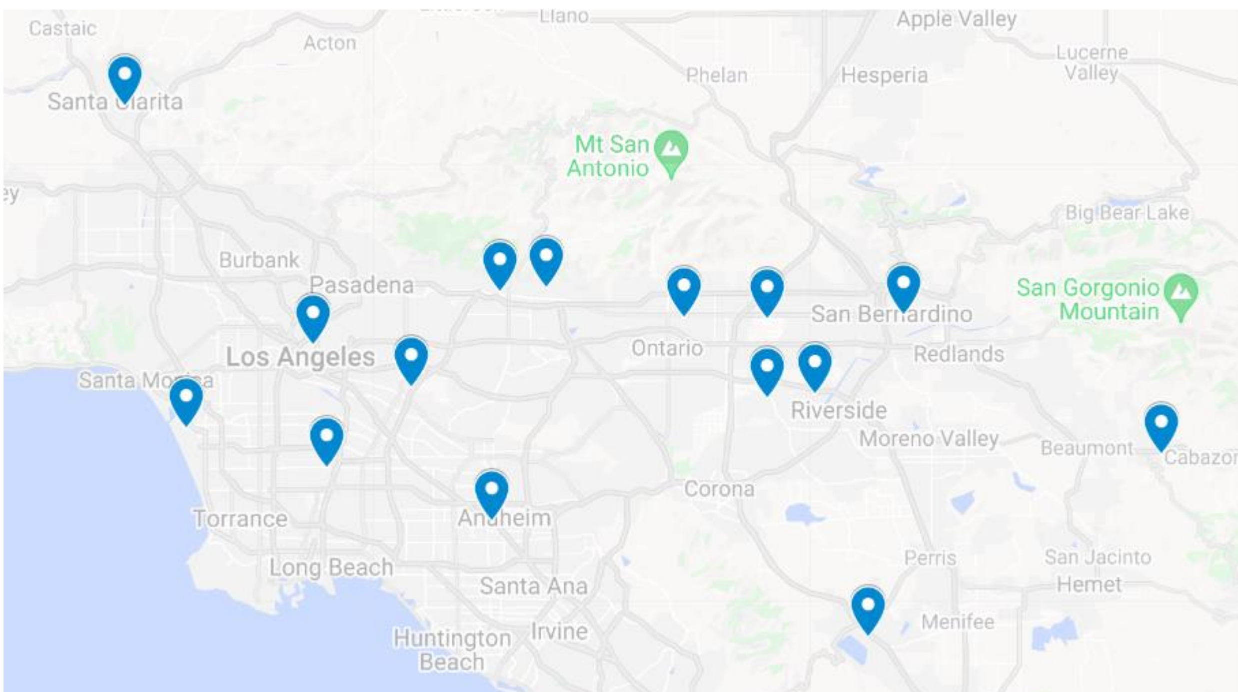


*Figure 2. Data from 15 air monitoring stations (Anaheim, Azusa, Banning, Compton, Fontana, Glendora, Lake Elsinore, LAX, LA North Main Street, Mira Loma, Rubidoux, San Gabriel, Santa Clarita, San Bernardino, Upland) were used for ML model predictions of ozone concentrations.*

# 3. Methods

We carried out a parallel approach using both ML and CMAQ to predict 2-D ozone concentrations as shown in Figure 4. The deterministic model (top panel) utilized WRF and CMAQ to simulate ozone concentrations based on a set of emissions and meteorology inputs. In contrast, the ML model (bottom panel) relied on observational meteorology and air quality data to predict ozone concentrations. ML and CMAQ models are evaluated with observational data to assess their performance, especially in response to the irregular emissions patterns of 2020. Additionally, predictions from ML and interpolation were explored to examine the NOx and VOC limited regimes in Southern California, providing insights into how the models perform in different regions.

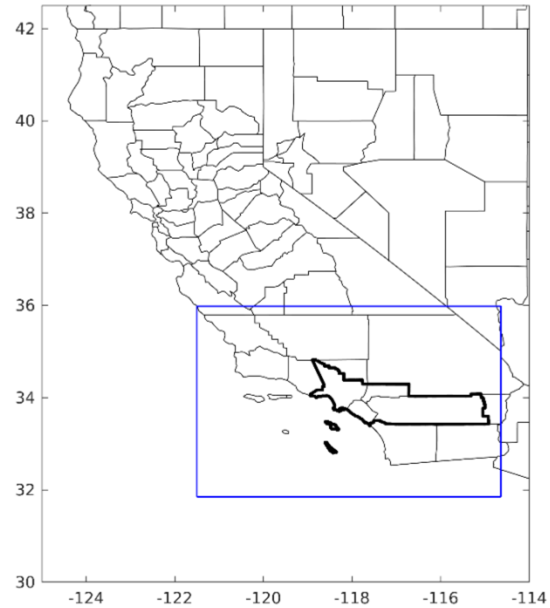


*Figure 3. The third and inner-most domain (blue boundary) with 4 km horizontal grid spacing covered the entire SCAQMD region (thick black lines).*

## 3.1 CMAQ Modeling

In this study, we compared the performance of both CMAQ and ML with spatial interpolations of ozone concentrations in SoCAB for the year 2020. The CMAQ simulation covered three distinct periods to study the impact of COVID-19 lockdown on air pollutant concentrations: pre-lockdown (Jan 1$^{st}$ to Mar 18$^{th}$), lockdown (Mar 16$^{th}$ to May 15$^{th}$), and post-lockdown (after May 16$^{th}$) periods. Meteorological modeling was carried out using the Weather Research and Forecasting (WRF) model version 3.9 with 4 km horizontal grid spacing, 11 vertical layers for the finest domain (10 layers near the surface), and 156 x 102 grid cells (Figure 3). There were two parent domains with coarser horizontal grid spacing (36 km and

12 km for domain 1 and domain 2, respectively). WRF configurations were optimized for SoCAB, and they included the use of USGS land use, thermal diffusion surface physics, and Yonsei University planetary boundary layer scheme (Hong et al., 2006; Huang et al., 2014). The CMAQ simulation used the modified 2020 emissions and previously described WRF simulations as inputs. The choice of chemical mechanism was SAPRC07tc_ae6_aq, i.e., SAPRC07tc photochemical mechanism, aerosol module 6, and aqueous chemistry (Byun & Schere, 2006; Carter, 2010).

## 3.2 Machine Learning

In a preceding study, we tested multiple ML algorithms to obtain a better method that resulted in the highest prediction accuracy for ozone concentrations in the SoCAB. Those included neural network, support vector machine, k-nearest neighbors, and random forest (Do et al., 2023). Here, we selected random forest regression (RFR), as RFR is the most suitable ML algorithm for predicting ozone concentrations in SoCAB (Do et al., 2023). For reference, RFR is a supervised learning algorithm with a tree-based ensemble method, i.e., a combination of multiple decision trees trained on an independent collection of input variables. In this application, RFR selected a random collection of features from the six input features for each decision tree to reduce bias, and the output of RFR is the average result from all decision trees (Rodriguez-Galiano et al., 2015; Zhang and Ma, 2012).

In this study, we selected six training features to predict ozone concentrations, which included two air quality features (NO and $NO_2$) and four meteorological features (temperature, relative humidity, wind speed, and wind direction). The two air quality features are directly related to ozone formation in the troposphere. Ozone undergoes the photolytic cycle during the day and is removed by NOx during nighttime (Brune, 2001; Liu et al., 1980; Trousdell et al., 2019). The four meteorological features were well studied in our previous work and were shown as the most important features to capture the variability in annual ozone, especially in SoCAB (Camalier et al., 2007; Gao et al., 2022; Jaffe, 2020).

We used the scikit-learn 0.22 library supported by the Python programming language to train our RFR model. Again, the input features are $NO_2$, NO, temperature, relative humidity, wind speed, and wind direction, and the label is ozone. We tuned the algorithm by varying the number of decision trees, the depth of the tree, sample split, and the sample leaf to obtain the best prediction accuracy. We used the same model tuning approached described in Do et al. (2023) (Table 2) (Do et al., 2023).

*Table 2. Optimal RFR configurations for the study*

| **Hyperparameter** | **Description** |
|---|---|
| n_estimators = 16 | The number of trees in the forest. |
| max_features = ‘auto’ | The number of features to consider when looking for the best split. |
| max_depth=None | The maximum depth of the tree. |
| min_samples_split=5 | The minimum number of samples required to split an internal node. |
| min_samples_leaf=30 | The minimum number of samples required to be at a leaf node. |
| min_weight_fraction_leaf=0 | The minimum weighted fraction of the sum total of weights required to be at a leaf node. |
| max_leaf_nodes=None | Best nodes are defined as relative reduction in impurity. |
| n_jobs=8 | The number of jobs to run in parallel. |

## 3.3 Spatial Interpolation

To generate a two-dimensional ozone concentration map, we first ran the RFR model to obtain the ozone concentrations at each air monitoring location (15 sites), which served as the model building sites. In other words, we applied a pointwise ML algorithm to predict ozone concentration at each trained location. Next, we spatially interpolated the output over the target Southern California region. We applied three different spatial interpolation methods (ordinary kriging, inverse distance weighting (IDW), and bicubic interpolation) and comparatively evaluated the performance of each method. Each interpolation approach is described below.

Ordinary kriging was applied to interpolate ozone concentration at the 10 km resolution over the study area. Ordinary kriging is a well-known spatial interpolation method developed by Danie G. Krige. Generally, kriging predicts the values for unknown locations by performing a series of linear combinations of values at known locations. Equation 1 expresses the generic form of the estimator to predict the optimum value $Z^*$of an unknown location by combining the known values $Z_i$ with their weights $\lambda_i$ (Oliver and Webster, 1990). We can write the variance $\sigma^2$ as an optimization problem (Eq. 2) that can be solved using the Lagrange multiplier $\mu$ (Eq. 3).

$$Z^*(u) = \sum_{i=1}^{n} \lambda_i Z(u_i) \tag{1}$$

$$\sigma^2(u) = Var[Z(u) - Z^*(u)] = -\sum_{j=1}^{n}\sum_{i=1}^{n} \lambda_j \lambda_i \gamma\left(u_i - u_j\right) + 2\sum_{i=1}^{n} \lambda_i \gamma(u_i - u) \tag{2}$$

$$\sum_{j=1}^{n} \lambda_j \left(u_i - u_j\right) + \mu = \gamma(u_i - u) \tag{3}$$

and

$$\sum_{j=1}^{n} \lambda_j = 1 \tag{4}$$

$\mu$ is the Lagrange multiplier, $u_i$ and $u_j$ are the distance of known locations from unknown locations $u$, $\gamma$ is the variogram, and $i = 1, \dots, n$. Equations 1 and 2 are called the kriging system, and $\lambda$ is the kriging weight. The values for $\lambda_i$ and the optimum value $Z^*$ are obtained by solving the kriging system and Equation 1 (Yamamoto, 2000).

Bicubic interpolation is another method for interpolating data points on a two-dimensional grid. The interpolated surface can be written in terms of two variables (Eq. 5). The polynomial $p$ consists of sixteen coefficients $a_{ij}$ that are solved with sixteen boundary conditions (i.e., $(x = 0, y = 0), (x = 1, y =$

0), $(x = 0, y = 1)$, $(x = 1, y = 1)$) and its derivatives with respect to $x$, $y$, and $xy$ (Seiler and Seiler, 1989).

$$p(x, y) = \sum_{i=0}^{3} \sum_{j=0}^{3} a_{ij} x^i y^j \tag{5}$$

The IDW interpolation method accounts for the distances between the interpolated points and the measured locations. The assumption for IDW is that points close to each other are more alike and have more significant influence than those farther apart. Thus, the nearest measured values have greater weights assigned. Equation 6 shows that the predicted value $Z(x)$ is inversely proportional to the distance between the measured and interpolated points $d(x, x_i)$.

$$Z(x) = \frac{\sum_{i=1}^{n} \frac{Z_i}{d(x, x_i)^p}}{\sum_{i=1}^{n} \frac{1}{d(x, x_i)^p}} \tag{6}$$

where $Z(x)$ is the predicted value, $d$ is the distance, $x$ is the unknown point, $x_i$ is the known location, $Z_i$ is the value of a known location, and $p$ is the power (Bartier and Keller, 1996).

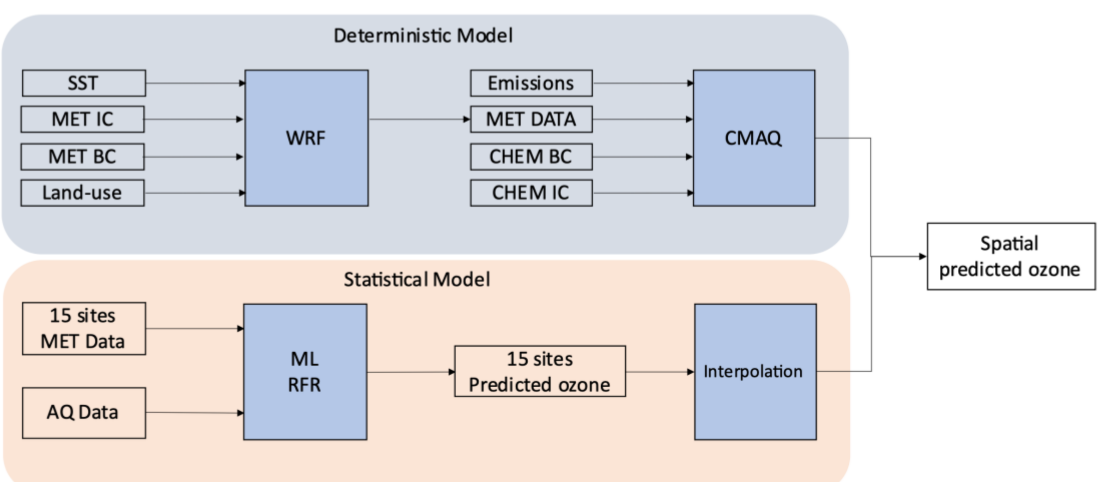


*Figure 4. Flow diagram of the deterministic (CMAQ) and ML models for predicting 2D ozone concentrations in Southern California, where SST is sea surface temperature, MET IC and MET BC are meteorology initial and boundary conditions, CHEM IC and CHEM BC are chemistry initial and boundary conditions, AQ Data is air quality data (NO and $NO_2$), MET Data is meteorology data (temperature, relative humidity, wind speed, and wind direction).*

# 4. Model Evaluation

Figure 5 shows a snapshot of the ozone concentrations over the interpolation region at 4:00 PM on June 22, 2020 (the highest ozone episode of the day), using ordinary kriging. The colored dots with a white border are the actual values at the evaluation sites, and those without a white border are the RFR predicted values for training sites. The model successfully reconstructed the spatial trends in the region where the lowest ozone levels were in the southwest (coastal) and the highest were in the east (inland), and there was good agreement with the actual ozone concentrations. Figures S2 and S3 show the heatmap for bicubic and IDW interpolation for the same timestamp. Although all interpolation methods predicted the lowest ozone concentrations in the Southwest, the highest ozone concentrations were predicted in the Northeast of the study region for bicubic and in the North for IDW. The concentration gradient increased from south to north for bicubic and IDW, but from west to east for ordinary kriging.

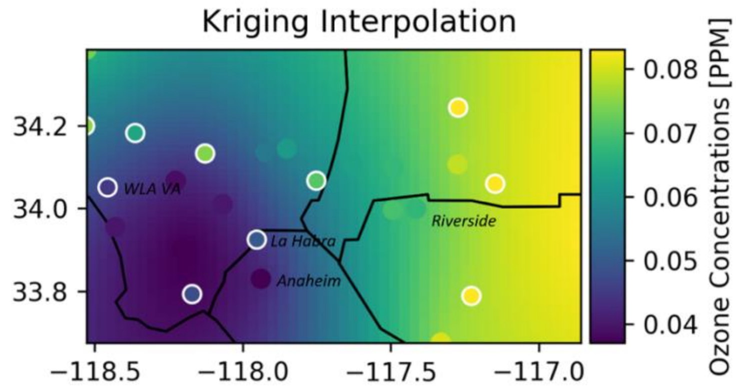


*Figure 55. Hourly ozone heatmap (16:00 on June 22, 2020) using ordinary kriging. The dots with white borders are the evaluation sites, and dots without borders are the training sites.*

The performance of the models was evaluated based on commonly used statistical metrics: mean bias (MB), correlation coefficient, root mean square error, and $R^2$ (equations listed in SI). The models were evaluated based on data from 27 air monitoring stations in SoCAB, of which 15 sites were used to evaluate the training sites, and the other 12 sites were used to evaluate the performance of the three interpolation methods at non-training sites. Table 3 and Table 4 highlight $R^2$ for daily average ozone for the bicubic, IDW, and ordinary kriging interpolations, as well as $R^2$ for the CMAQ comparison. We used the entire year to evaluate the interpolation methods, but we only used the five highest ozone months from May to September for the CMAQ evaluation.

*Table 3. Daily average $R^2$ at the 15 building sites for three interpolation methods for the year 2020. $R^2$ for CMAQ was computed using the five highest ozone months May - September of 2020.*

| Sites | Bicubic $R^2$ | IDW $R^2$ | Ordinary Kriging $R^2$ | CMAQ $R^2$ |
|---|---|---|---|---|
| Anaheim | 0.66 | 0.67 | 0.74 | 0.41 |
| Azusa | 0.52 | 0.64 | 0.77 | 0.59 |
| Banning | 0.17 | 0.46 | 0.73 | 0.26 |
| Compton | 0.65 | 0.67 | 0.77 | 0.48 |
| Fontana | 0.88 | 0.89 | 0.87 | 0.59 |
| Glendora | 0.46 | 0.53 | 0.72 | 0.52 |
| Lake Elsinore | 0.52 | 0.70 | 0.79 | 0.56 |
| LA North Main ST | 0.36 | 0.67 | 0.78 | 0.48 |
| LAX | 0.31 | 0.48 | 0.65 | 0.25 |
| Mira Loma | 0.56 | 0.71 | 0.86 | 0.67 |
| Rubidoux | 0.46 | 0.65 | 0.86 | 0.68 |
| San Bernardino | 0.68 | 0.85 | 0.86 | 0.67 |
| San Gabriel | 0.53 | 0.77 | 0.81 | 0.62 |
| Santa Clarita | 0.27 | 0.72 | 0.84 | 0.61 |
| Upland | 0.76 | 0.80 | 0.86 | 0.61 |

*Table 4. Daily average $R^2$ at 12 evaluation sites, and these were not used spatial interpolation. $R^2$ for CMAQ was computed using the five highest ozone months, May - September of 2020.*

| Sites | Bicubic $R^2$ | IDW $R^2$ | Ordinary Kriging $R^2$ | CMAQ $R^2$ |
|---|---|---|---|---|
| Crestline | 0.35 | 0.42 | 0.42 | 0.23 |
| La Habra | 0.75 | 0.80 | 0.77 | 0.44 |
| Long Beach | 0.46 | 0.60 | 0.56 | 0.30 |
| Mission Viejo | 0.15 | 0.36 | 0.49 | 0.39 |
| North Hollywood | 0.67 | 0.67 | 0.79 | 0.59 |
| Pasadena | 0.55 | 0.71 | 0.78 | 0.57 |
| Perris | 0.55 | 0.72 | 0.80 | 0.56 |
| Pomona | 0.71 | 0.83 | 0.84 | 0.68 |
| Redlands | 0.60 | 0.74 | 0.71 | 0.57 |
| Reseda | 0.63 | 0.63 | 0.71 | 0.01 |
| West LA | 0.29 | 0.56 | 0.60 | 0.28 |
| Winchester | 0.37 | 0.40 | 0.39 | 0.45 |

The bicubic $R^2$ indicates the poorest performance of the three interpolation methods. The lowest $R^2$ values for the 12 evaluation sites were 0.15 and 0.29, Mission Viejo and West LA, respectively (Table

4). The poor performance resulted from the method used to calculate the coefficients $a_{ij}$ (Eq. 5), for which the values of coefficients did not depend on the distance between interpolating points but were dependent on the formation of a smooth curve. Bicubic is best for evenly distributed points, such as interpolating image pixels. IDW showed a significant improvement compared to bicubic interpolation. The lowest $R^2$ was 0.36 for Mission Viejo, and the highest $R^2$ was 0.83 for Pomona. Since IDW accounts for the distances between the interpolation points and the data points, farther data points have less influence on the interpolation points. Ordinary kriging resulted in the best interpolation method, with the lowest $R^2$ of 0.39 for Winchester and the highest $R^2$ of 0.84 for Pomona. Kriging not only accounts for the distance between building points and interpolated data by assigning larger weight $\lambda_i$ to the near neighbors, but it also considers the variability of data by considering the variance of input data, $\sigma^2$. The basis of the variogram function represents the spatial variability of data. The variance depends not on observation values but on the variogram model and geometry (Kebaili Bargaoui and Chebbi, 2009) (Eq. 2).

ML with interpolation gave a poor performance for Crestline and Winchester locations. Crestline is located in the mountains and to the northeast of SoCAB, which is elevated terrain associated with upper air and a different air mass at times. Crestline ozone was not well-correlated with coastal or inland sites. Thus, interpolated Crestline ozone based on coastal or inland data points will likely yield poor results. The Winchester air monitoring site is located near the Skinner Reservoir (Figure S1), far away from other data points (Lake Elsinore and Banning). Low $R^2$ for Winchester can be explained by the influence of the lake and local meteorology and air quality. The ordinary kriging model performed well for locations bounded by data points with $R^2$ above 0.56. However, poor interpolation results occurred for peripheral locations in SoCAB (Crestline, Mission Viejo, and Winchester). LAX ozone levels were not well correlated with meteorology, and training the ML model with fewer meteorological features did not affect the performance of the LAX location. Overall, model performance increased from the West to the East, with better prediction for inland sites.

The distribution of the monthly mean bias (MB) for ordinary kriging interpolation centered around zero with the range between +9 ppb for Compton (August) and -11 ppb for Glendora (October). Eleven building sites have a net positive monthly MB, and four have a net negative monthly MB (Figure 6). The results from the CMAQ simulation overestimated the ozone levels. CMAQ's best performance was from May to October when the MBs were the smallest. In general, ozone concentrations in the SoCAB are highest during the summer and lowest in the winter, corresponding with the temperature. Even though the CMAQ simulation captures diurnal variation, the seasonal variation is not as well-represented (Figure S4, S5, S7, and S11). Lower performing CMAQ results could come from uncertainties in emissions estimates. CMAQ generally overestimated ozone concentrations because the simulated nighttime ozone concentrations were higher than those observed, potentially due to underestimated nighttime $NO_X$ emissions (Zhu et al., 2023). In other words, that there was not enough NOx emitted in the model during the daytime for ozone formation and at night for ozone removal (Awang and Ramli, 2017; Brown et al., 2004).

Training features can be varied to study the sensitivity to modeled ozone response. For example, we can perturb the temperature, RH, or emissions values and examine the ozone levels corresponding to the change in the features. However, because the formation of ozone results from a complex combination of chemical reactions, resulting impacts are nonlinear and interdependent. Therefore, when using ML to test for sensitivity to a feature, one should consider feature dependencies. For example, in testing temperature impacts on ozone concentration, we must consider both how temperature impacts photolysis rates ($NO_2$ degradation) as well as simultaneous correlations/anticorrelation with other meteorological variables, such as RH or wind speed.

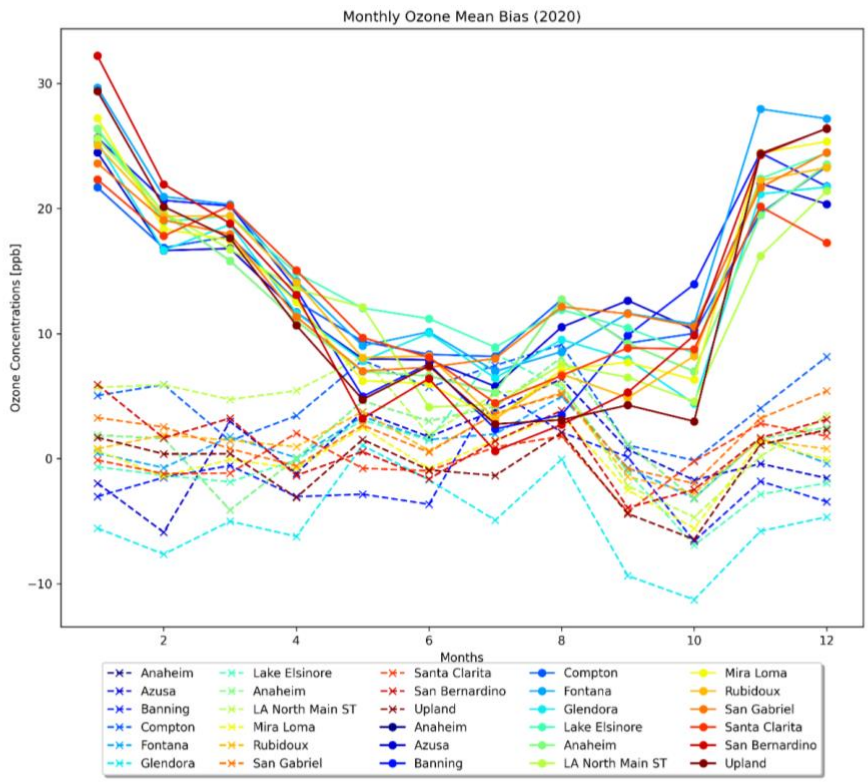


*Figure 6. Monthly mean bias computed for 2020 for 15 sites using the kriging interpolation method (dash lines), and CMAQ simulation (solid lines). The colors of the lines correspond to the evaluation locations.*

# 5. Discussion

The reduction in traffic volumes during the lockdown from March to May led to a decrease in observed CO and $NO_X$ (Ivey et al., 2020; Tanvir et al., 2023). As a result, we expected an overall reduction in ozone levels over the SoCAB region. The average diurnal ozone concentrations before the lockdown (Jan - Feb) in 2020 were noticeably greater than the average from 2016 – 2019 for all 15 building sites. Figure 7 shows the averaged diurnal profiles of three 2020 periods for inland sites, Lake Elsinore and Fontana: pre-lockdown (a, d), lockdown (b, e), and post-lockdown (c, f) periods. Before the lockdown, the 2020 ozone concentrations (red line) in Lake Elsinore and Fontana exceeded the four-year average (blue line), indicating a recent worsening of ozone trends in Southern California. The ML model with the interpolation method (black line) successfully predicted this ozone trend before the lockdown. During the lockdown, observed ozone levels in 2020 significantly decreased in Lake Elsinore, dropping below the four-year average. After the lockdown, ozone levels in 2020 rebounded but remained lower than the pre-lockdown period. The ML model effectively captured these ozone trends throughout the three periods of 2020 for the Lake Elsinore site. In contrast, ozone levels in Fontana did not decrease significantly below the four-year average during the lockdown and remained high afterward. It is important to note that Lake Elsinore is located in a remote area surrounded by trees. During the lockdown, Lake Elsinore showed a drop in ozone concentrations, indicating that the location is in a $NO_x$ limited atmosphere, where fluctuations in $NO_x$ have a significant impact on ozone levels. On the other hand, Fontana is an urban site, and the ozone levels did not exhibit significant improvement during the lockdown, suggesting that Fontana is located in a VOC limited regime.

Post-lockdown differences compared to the four-year average were not significant across the 15 sites. The RFR model captured ozone trends throughout 2020, although slightly lower during and despite the observed reduction in NOx, suggesting that meteorological features would play an important role in predicting ozone levels during anomalous episodes in addition to air quality features. Actual and modeled discrepancies also indicate anomalous ozone behavior during lockdown. For instance, several sites in the SoCAB showed an increase in ozone levels based on the diurnal profile implying that the urban locations in the SoCAB were VOCs-limited regimes, where reduction in NOx reduction-initiated ozone enhancement (Parker et al., 2020).

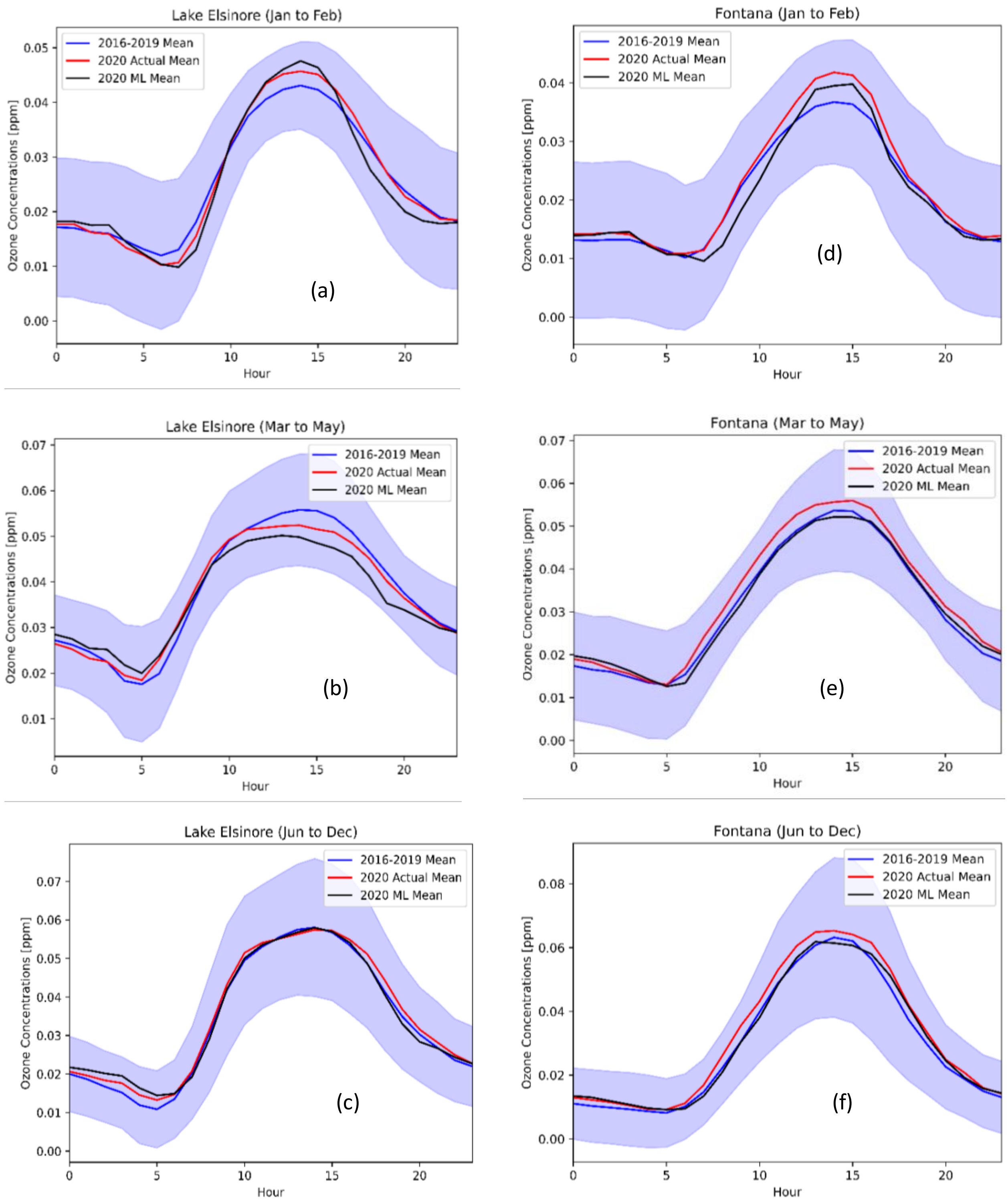


*Figure 77. Averaged diurnal profiles of 2016 - 2019 (blue), actual 2020 (red), and ML predicted 2020 (black) ozone concentrations (ppm) at Lake Elsinore (a, b, c) and Fontana (d, e, f) for three different periods: (a,d) pre-lockdown (Jan to Feb), (b,e) lockdown (Mar to May), and (c,f) post-lockdown (after May). The shaded area is the standard deviation of the 2016 - 2019 measurements. Additional sites are provided in the SI.*

# 6. Conclusion

This study highlights the advantages of spatial interpolation methods for ozone predictions during anomalous environmental events. With modern processor architectures (e.g., AMD Zen 3 or Intel Alder Lake), training the RFR model and performing high-resolution interpolation over the SoCAB region for one prediction year took less than five minutes of walltime with a 16-core processor. In contrast, CMAQ walltime was 16 days for a year-long simulation for the SoCAB region. Further, ozone modeling for 2020 was challenging because of expected emissions conditions from March to September, during which traffic volume significantly decreased (up to 40% reduction in some locations). We hypothesized that mid-2020 ozone levels would decrease semi-proportionally due to the decline in traffic volume. However, the changes in ozone levels in the SoCAB were small in magnitude, but directionally the changes were informative for future emissions reductions planning (increased ozone indicates VOC limitations). Ordinary kriging interpolation using ML building provided daily data, addressed data missingness, and captured 2020 ozone trends with fairly low bias despite the sudden change in emissions. The ML model with the interpolation method successfully captured ozone trends throughout three periods in 2020, particularly in locations operating under a $NO_x$ limited regime, such as Lake Elsinore. However, it faced challenges in predicting ozone levels during the lockdown period in areas characterized by a VOC limited regime, like Fontana. ML inherently relies on patterns learned from historical data to make predictions, especially for inputs that resemble past occurrences. In this study, the ML model struggled to make accurate predictions for VOC limited regime, suggesting that events akin to the COVID-19 lockdown had not been encountered in the past. Unfortunately, due to the unavailability of speciated VOC data, we didn’t incorporate them as a training feature in the model. Since ozone formation exhibits a non-linear correlation with both $NO_x$ and VOC, the inclusion of speciated VOC data would likely enhance the model's accuracy, especially for regions with both $NO_x$ and VOC limited regimes. Our ML model provides regulators with valuable insights into $NO_x$ and VOC limited regimes across the Southern California domain, enabling policymakers to devise more effective emission reduction strategies and improve air quality at hyperlocal scales.

## Data and Source Codes

All training and evaluating air quality and meteorology data are available at https://aqs.epa.gov/aqsweb/airdata/download_files.html#Raw. Weekly traffic observations in Southern California and emissions are available upon request. Source codes for ML and interpolation were uploaded to GitHub: https://github.com/kdo037/Machine-Learning-with-Spatial-Interpolation.

## Acknowledgment

This paper was prepared as a result of work sponsored, paid for in part by, the South Coast Air Quality Management District (SCAQMD). The opinions, findings, conclusions, and recommendations are those of the authors and do not necessarily represent the views of SCAQMD. We acknowledge Graduate Assistant in Areas of Need (GAANN) support from the University of California, Riverside Chemical and Environmental Department. The authors thank the South Coast Air Quality Management District for providing emissions data and Dwaraknath Ravichandran and Prof. Shams Tanvir, who provided 2020 traffic data for emission correction. The authors acknowledge partial support from the University of California Institute for Transportation Studies for work conducted for this manuscript. The authors thank Prof. Armistead G. Russell and Dr. Charles L. Blanchard for their guidance on this work.

# References


Apte, J.S., Messier, K.P., Gani, S., Brauer, M., Kirchstetter, T.W., Lunden, M.M., Marshall, J.D., Portier, C.J., Vermeulen, R.C.H., Hamburg, S.P., 2017. High-Resolution Air Pollution Mapping with Google Street View Cars: Exploiting Big Data. Environmental Science and Technology 51, 6999–7008. https://doi.org/10.1021/acs.est.7b00891

Awang, N.R., Ramli, N.A., 2017. Preliminary Study of Ground Level Ozone Nighttime Removal Process in an Urban Area. Journal of Tropical Resources and Sustainable Science (JTRSS) 5. https://doi.org/10.47253/jtrss.v5i2.595

Bartier, P.M., Keller, C.P., 1996. Multivariate interpolation to incorporate thematic surface data using inverse distance weighting (IDW). Computers & Geosciences 22, 795–799. https://doi.org/10.1016/0098-3004(96)00021-0

Brown, S.S., Dibb, J.E., Stark, H., Aldener, M., Vozella, M., Whitlow, S., Williams, E.J., Lerner, B.M., Jakoubek, R., Middlebrook, A.M., DeGouw, J.A., Warneke, C., Goldan, P.D., Kuster, W.C., Angevine, W.M., Sueper, D.T., Quinn, P.K., Bates, T.S., Meagher, J.F., Fehsenfeld, F.C., Ravishankara, A.R., 2004. Nighttime removal of NOx in the summer marine boundary layer. Geophysical Research Letters 31. https://doi.org/10.1029/2004GL019412

Brune, W.H., 2001. Introduction to Atmospheric Chemistry: Daniel J. Jacob; Princeton University Press, Princeton, NJ, 1999, 266pp., ISBN 0-691-00185-5. Atmospheric Environment 35, 1715. https://doi.org/10.1016/S1352-2310(00)00432-5

California Air Resources Board, 2023. Trends Summary [WWW Document]. URL https://www.arb.ca.gov/adam/trends/trends1.php

Caltrans, 2023. Caltrans PeMS [WWW Document]. URL https://dot.ca.gov/programs/traffic-operations/census/mvmt

Camalier, L., Cox, W., Dolwick, P., 2007. The effects of meteorology on ozone in urban areas and their use in assessing ozone trends. Atmospheric Environment 41, 7127–7137. https://doi.org/10.1016/j.atmosenv.2007.04.061

Do, K., Manasi, M., Kashfi Yeganeh, A., Gao, Z., Blanchard, C.L., Ivey, C.E., 2023. A Machine Learning Approach to Quantify the Impact of Meteorology on Tropospheric Ozone in the Inland Empire, CA. Accepted in Environmental Science: Atmospheres.

Gao, Z., Ivey, C.E., Blanchard, C.L., Do, K., Lee, S.-M., Russell, A.G., 2022. Separating emissions and meteorological impacts on peak ozone concentrations in Southern California using generalized additive modeling. Environmental Pollution 307, 119503. https://doi.org/10.1016/j.envpol.2022.119503

Ivey, C., Gao, Z., Do, K., Kashfi Yeganeh, A., Russell, A., Blanchard, C.L., Lee, S.-M., 2020. Impacts of the 2020 COVID-19 Shutdown Measures on Ozone Production in the Los Angeles Basin (preprint). https://doi.org/10.26434/chemrxiv.12805367.v1

Jaffe, D., 2020. Role of Meteorology, Emissions and Smoke on Ozone in the South Coast Air Basin, Final project report for CRC Project A-118. Coordinating Research Council, Alpharetta, GA.

Jiang, Z., Shi, H., Zhao, B., Gu, Y., Zhu, Y., Miyazaki, K., Lu, X., Zhang, Y., Bowman, K.W., Sekiya, T., Liou, K.-N., 2021. Modeling the impact of COVID-19 on air quality in southern California: implications for future control policies. Atmos. Chem. Phys. 21, 8693–8708. https://doi.org/10.5194/acp-21-8693-2021

Joseph, J., Sharif, H.O., Sunil, T., Alamgir, H., 2013. Application of validation data for assessing spatial interpolation methods for 8-h ozone or other sparsely monitored constituents. Environmental Pollution 178. https://doi.org/10.1016/j.envpol.2013.03.035

Karamchandani, P., Morris, R., Wentland, A., Shah, T., Reid, S., Lester, J., 2017. Dynamic Evaluation of Photochemical Grid Model Response to Emission Changes in the South Coast Air Basin in California. Atmosphere 8, 145. https://doi.org/10.3390/atmos8080145

Kebaili Bargaoui, Z., Chebbi, A., 2009. Comparison of two kriging interpolation methods applied to spatiotemporal rainfall. Journal of Hydrology 365, 56–73. https://doi.org/10.1016/j.jhydrol.2008.11.025

Liu, S.C., Kley, D., McFarland, M., Mahlman, J.D., Levy, H., 1980. On the origin of tropospheric ozone. Journal of Geophysical Research. https://doi.org/10.1029/jc085ic12p07546

Lurmann, F., Avol, E., Gilliland, F., 2015. Emissions reduction policies and recent trends in Southern California’s ambient air quality. Journal of the Air & Waste Management Association 65, 324–335. https://doi.org/10.1080/10962247.2014.991856

Miyasato, M., Tisopulos, L., Low, J., Bermudez, R., Vlasich, B., 2016. Annual Air Quality Monitoring Network Plan.

Oliver, M.A., Webster, R., 1990. Kriging: A method of interpolation for geographical information systems. International Journal of Geographical Information Systems 4. https://doi.org/10.1080/02693799008941549

Parker, H.A., Hasheminassab, S., Crounse, J.D., Roehl, C.M., Wennberg, P.O., 2020. Impacts of Traffic Reductions Associated With COVID-19 on Southern California Air Quality. Geophys. Res. Lett. 47. https://doi.org/10.1029/2020GL090164

Rodriguez-Galiano, V., Sanchez-Castillo, M., Chica-Olmo, M., Chica-Rivas, M., 2015. Machine learning predictive models for mineral prospectivity: An evaluation of neural networks, random forest, regression trees and support vector machines. Ore Geology Reviews. https://doi.org/10.1016/j.oregeorev.2015.01.001

Seiler, M.C., Seiler, F.A., 1989. Numerical Recipes in C: The Art of Scientific Computing. Risk Analysis 9. https://doi.org/10.1111/j.1539-6924.1989.tb01007.x

South Coast Air Quality Management District, 2017. Final 2016 Air Quality Management Plan.

Tanvir, S., Ravichandran, D., Ivey, C., Barth, M., Boriboonsomsin, K., 2023. Traffic, Air Quality, and Environmental Justice in the South Coast Air Basin During California’s COVID-19 Shutdown, in: Loukaitou-Sideris, A., Bayen, A.M., Circella, G., Jayakrishnan, R. (Eds.), Pandemic in the Metropolis. Springer International Publishing, Cham, pp. 131–148. https://doi.org/10.1007/978-3-031-00148-2_9

Trousdell, J.F., Caputi, D., Smoot, J., Conley, S.A., Faloona, I.C., 2019. Photochemical production of ozone and emissions of NOx and CH4 in the San Joaquin Valley. Atmospheric Chemistry and Physics. https://doi.org/10.5194/acp-19-10697-2019

Wang, W., Bruyere, C., Duda, M., Dudhia, J., Gill, D., Kavulich, M., Keene, K., Chen, M., Lin, H.-C., Michalakes, J., Rizvi, S., Zhang, X., Berner, J., Ha, S., Fossell, K., 2017. WRF Version 3.9 User’s Guide.

Wong, D.W., Yuan, L., Perlin, S.A., 2004. Comparison of spatial interpolation methods for the estimation of air quality data. Journal of Exposure Analysis and Environmental Epidemiology. https://doi.org/10.1038/sj.jea.7500338

Yu, H., Russell, A., Mulholland, J., Odman, T., Hu, Y., Chang, H.H., Kumar, N., 2018. Cross-comparison and evaluation of air pollution field estimation methods. Atmospheric Environment. https://doi.org/10.1016/j.atmosenv.2018.01.045

Zhang, C., Ma, Y., 2012. Ensemble machine learning: Methods and applications, Ensemble Machine Learning: Methods and Applications. https://doi.org/10.1007/9781441993267

Zhu, S., Horne, J.R., Mac Kinnon, M., Samuelsen, G.S., Dabdub, D., 2019. Comprehensively assessing the drivers of future air quality in California. Environment International 125, 386–398. https://doi.org/10.1016/j.envint.2019.02.007

Zhu, Z., Do, K., Ibarra Gomez, D., Ivey, C.E., Collins, D., 2023. Assessing CMAQ Model Discrepancies in Vertical Ozone Profiles in a Heavily-Polluted Air Basin using UAV Measurements. In preparation.

Supplemental Information for:

# Performance of Machine Learning for Ozone Modeling in Southern California during the COVID-19 Shutdown

Khanh Do[1,2], Arash Kashfi Yeganeh[1,2], Ziqi Gao[3], Cesunica E. Ivey[1,2,4*]

*Corresponding Author: iveyc@berkeley.edu

[1]Department of Chemical and Environmental Engineering, University of California Riverside, Riverside, CA, USA

[2]Center for Environmental Research and Technology, Riverside, CA, USA

[3]Department of Civil and Environmental Engineering, Georgia Institute of Technology, Atlanta, GA, USA

[4]Now at Department of Civil and Environmental Engineering, University of California, Berkeley, Berkeley, CA, USA

Evaluation Metrics

Correlation coefficient

$$CC = \frac{\sum_{i=1}^{N}(M_i - \bar{M})(O_i - \bar{O})}{[\sum_{i=1}^{N}(M_i - \bar{M})^2 \sum_{i=1}^{N}(O_i - \bar{O})^2]^{\frac{1}{2}}} \tag{1}$$

Mean bias:

$$MB = \frac{1}{N}\sum_{i=1}^{N}(M_i - O_i) \tag{2}$$

Mean absolute error:

$$MAE = \frac{1}{N}\sum_{i=1}^{N}|M_i - O_i| \tag{3}$$

Root mean square error:

$$RMSE = [\frac{1}{N}\sum_{i=1}^{N}(M_i - O_i)^2]^{\frac{1}{2}} \tag{4}$$

Relative root mean square error:

$$rRMSE = \frac{[\frac{1}{N}\sum_{i=1}^{N}(M_i - O_i)^2]^{\frac{1}{2}}}{\frac{1}{N}\sum_{i=1}^{N}O_i} \tag{5}$$

Mean normalized bias:

$$MNB = \frac{1}{N}\sum_{i=1}^{N}\frac{M_i - O_i}{O_i} \tag{6}$$

Mean normalized absolute error:

$$MNAE = \frac{1}{N}\sum_{i=1}^{N}\frac{|M_i - O_i|}{O_i} \tag{7}$$

Normalized mean bias:

$$NMB = \frac{\sum_{i=1}^{N}(M_i - O_i)}{\sum_{i=1}^{N}O_i} \tag{8}$$

Normalized mean absolute error:

$$NMAE = \frac{\sum_{i=1}^{N}|M_i - O_i|}{\sum_{i=1}^{N}O_i} \tag{9}$$

Fractional bias:

$$FB = \frac{1}{N}\sum_{i=1}^{N}\frac{M_i - O_i}{(M_i + O_i)/2} \tag{10}$$

Fractional absolute error:

$$FAE = \frac{1}{N}\sum_{i=1}^{N}\frac{|M_i - O_i|}{(M_i + O_i)/2} \tag{11}$$

Model mean:

$$\bar{M} = \frac{1}{N}\sum_{i=1}^{N} M_i \tag{12}$$

Observational mean:

$$\bar{O} = \frac{1}{N}\sum_{i=1}^{N} O_i \tag{13}$$

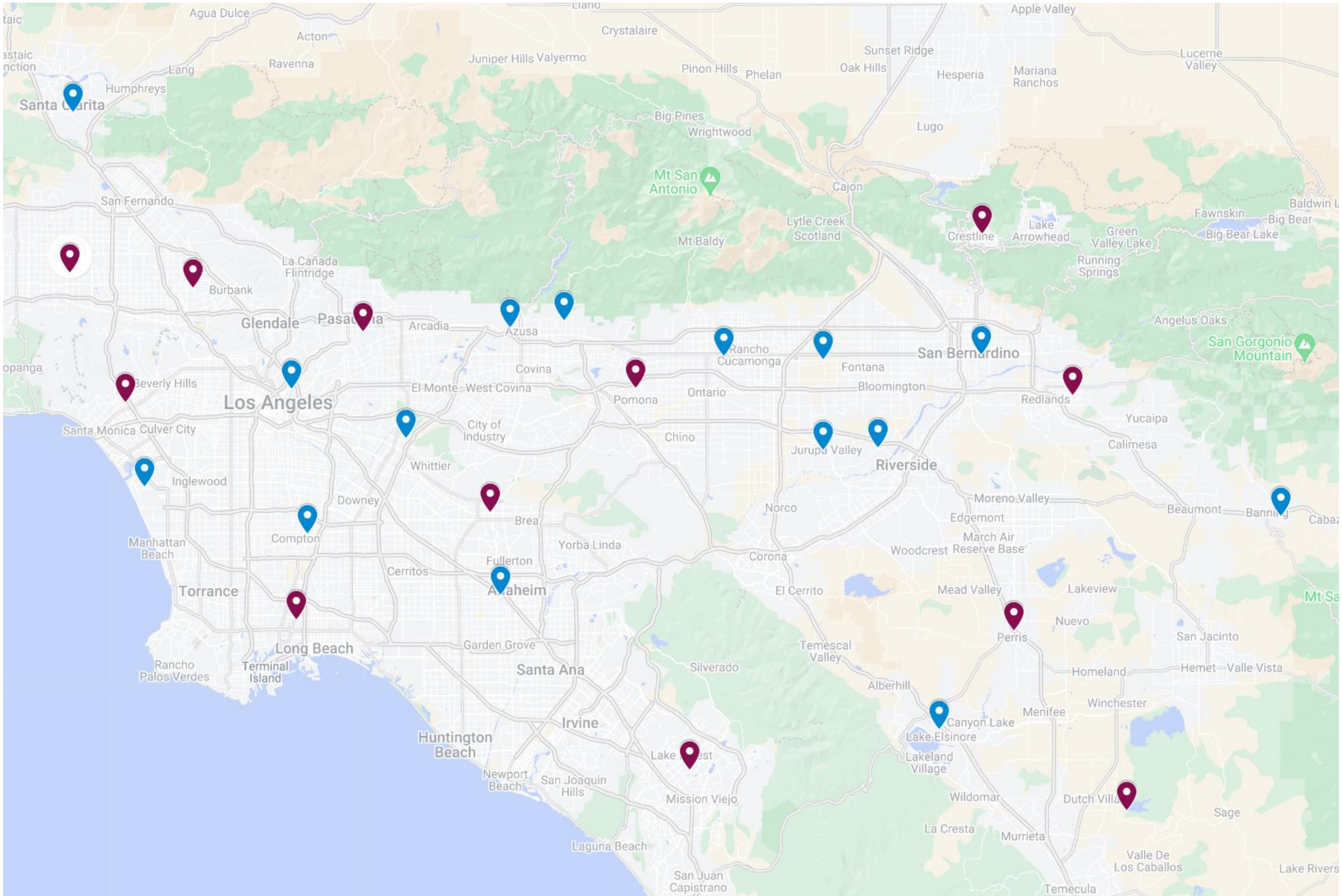


*Figure S1. The map shows 27 air monitoring sites in the SoCAB. Blue labels were used for interpolation points, and red labels were used for interpolation performance evaluation.*

*Table S1. The R2 for CMAQ was computed for the entire year of 2020.*

| Sites | 2020 CMAQ $R^2$ |
|---|---|
| Anaheim | 0.24 |
| Azusa | 0.39 |
| Banning | 0.17 |
| Compton | 0.38 |
| Fontana | 0.36 |
| Glendora | 0.37 |
| Lake Elsinore | 0.43 |
| LA North Main ST | 0.26 |
| LAX | 0.17 |
| Mira Loma | 0.48 |
| Rubidoux | 0.52 |
| San Bernardino | 0.50 |
| San Gabriel | 0.48 |
| Santa Clarita | 0.43 |
| Upland | 0.36 |
| Crestline | 0.22 |
| La Habra | 0.27 |
| Long Beach | 0.15 |
| Mission Viejo | 0.19 |
| North Hollywood | 0.36 |
| Pasadena | 0.32 |
| Perris | 0.47 |
| Pomona | 0.55 |
| Redlands | 0.43 |
| Reseda | 0.36 |
| West LA | 0.18 |
| Winchester | 0.30 |

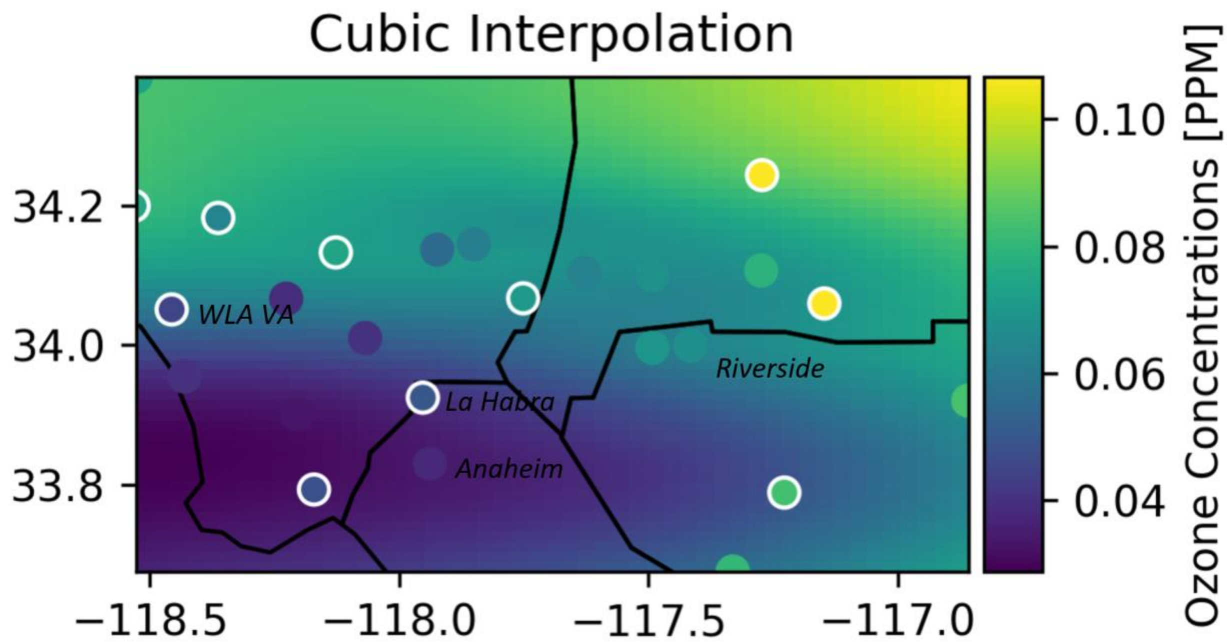


*Figure S2. Hourly ozone heatmap (@16pm June 22, 2020) using cubic interpolation.*

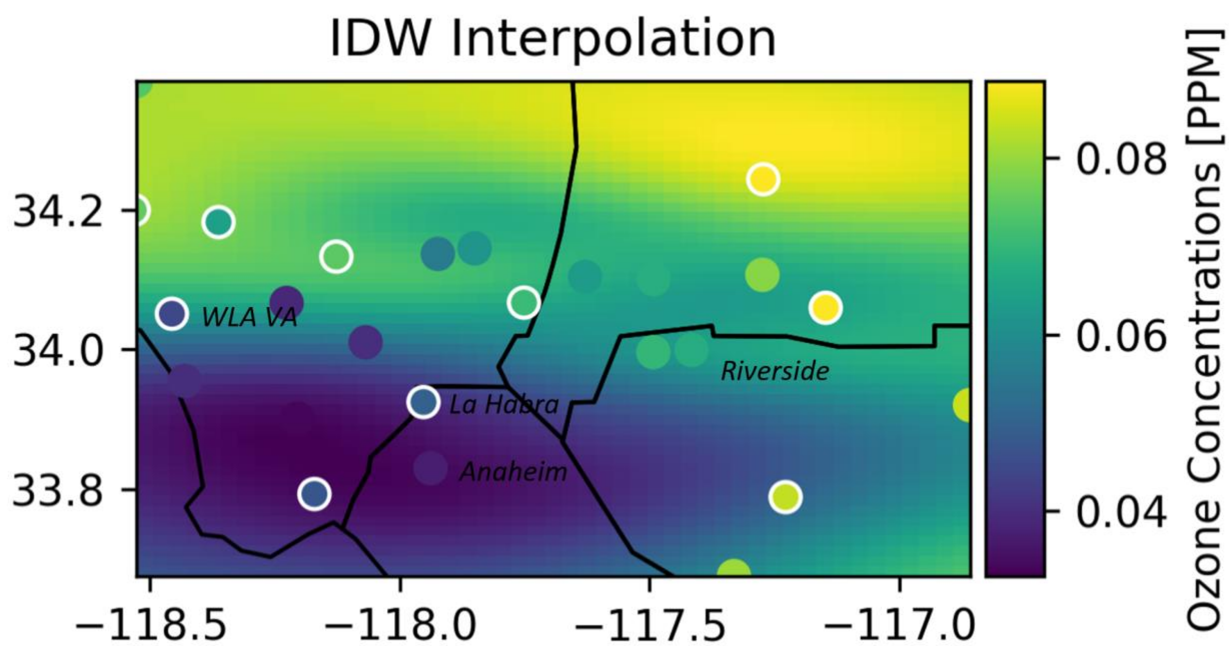


*Figure S3. Hourly ozone heatmap (@16pm June 22, 2020) using IDW interpolation.*

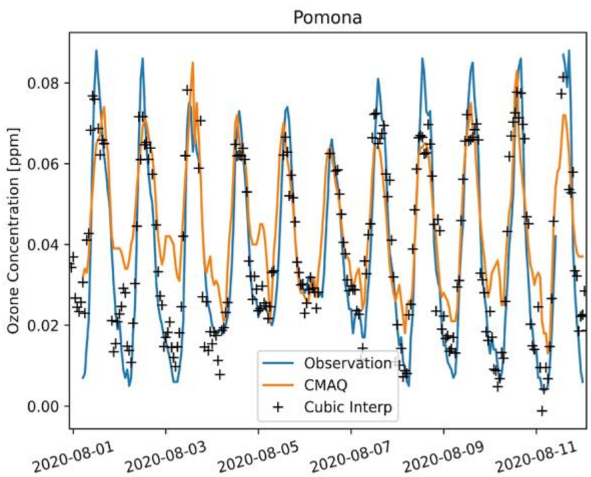


*Figure S4. Time series plotting ozone concentrations for CMAQ model, cubic interpolation, and observation*

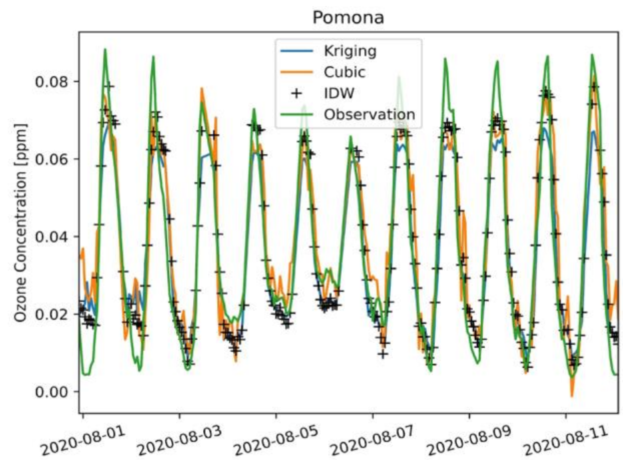


*Figure S5. Time series plotting ozone concentrations for three different interpolation methods (kriging, cubic, and IDW) with observation*

*Table S2. Evaluation was computed using the average of 12 evaluation sites.*

| Month | CC | MB | MAGE | RMSE | MNB | MNAE | NMB | NMAE | FB | FAE | MM | OM |
|---|---|---|---|---|---|---|---|---|---|---|---|---|
| 1 | 0.40 | 0.01 | 0.01 | 0.02 | 7.26 | 7.42 | 0.58 | 0.88 | 0.71 | 0.93 | 0.03 | 0.02 |
| 2 | 0.26 | 0.00 | 0.01 | 0.02 | 4.56 | 4.77 | 0.16 | 0.44 | 0.33 | 0.59 | 0.03 | 0.03 |
| 3 | 0.75 | 0.01 | 0.01 | 0.02 | 6.71 | 6.79 | 0.78 | 0.97 | 0.94 | 1.04 | 0.03 | 0.01 |
| 4 | 0.62 | 0.00 | 0.01 | 0.01 | 1.73 | 1.98 | 0.00 | 0.30 | 0.10 | 0.40 | 0.03 | 0.03 |
| 5 | 0.85 | 0.00 | 0.01 | 0.01 | 0.44 | 0.61 | 0.05 | 0.25 | 0.13 | 0.34 | 0.03 | 0.03 |
| 6 | 0.83 | 0.00 | 0.01 | 0.01 | 0.47 | 0.73 | -0.03 | 0.23 | -0.01 | 0.31 | 0.04 | 0.04 |
| 7 | 0.80 | 0.01 | 0.01 | 0.02 | 1.08 | 1.24 | 0.13 | 0.34 | 0.28 | 0.48 | 0.04 | 0.04 |
| 8 | 0.81 | 0.00 | 0.01 | 0.02 | 1.96 | 2.21 | 0.14 | 0.36 | 0.20 | 0.50 | 0.04 | 0.03 |
| 9 | 0.62 | 0.01 | 0.02 | 0.02 | 5.88 | 6.16 | 0.19 | 0.59 | 0.40 | 0.76 | 0.04 | 0.03 |
| 10 | 0.35 | 0.01 | 0.02 | 0.02 | 5.94 | 6.19 | 0.35 | 0.71 | 0.45 | 0.76 | 0.03 | 0.02 |
| 11 | 0.49 | 0.01 | 0.01 | 0.02 | 5.61 | 5.76 | 0.43 | 0.71 | 0.63 | 0.82 | 0.03 | 0.02 |
| 12 | 0.39 | 0.00 | 0.01 | 0.01 | 3.15 | 3.37 | 0.22 | 0.55 | 0.40 | 0.67 | 0.03 | 0.02 |

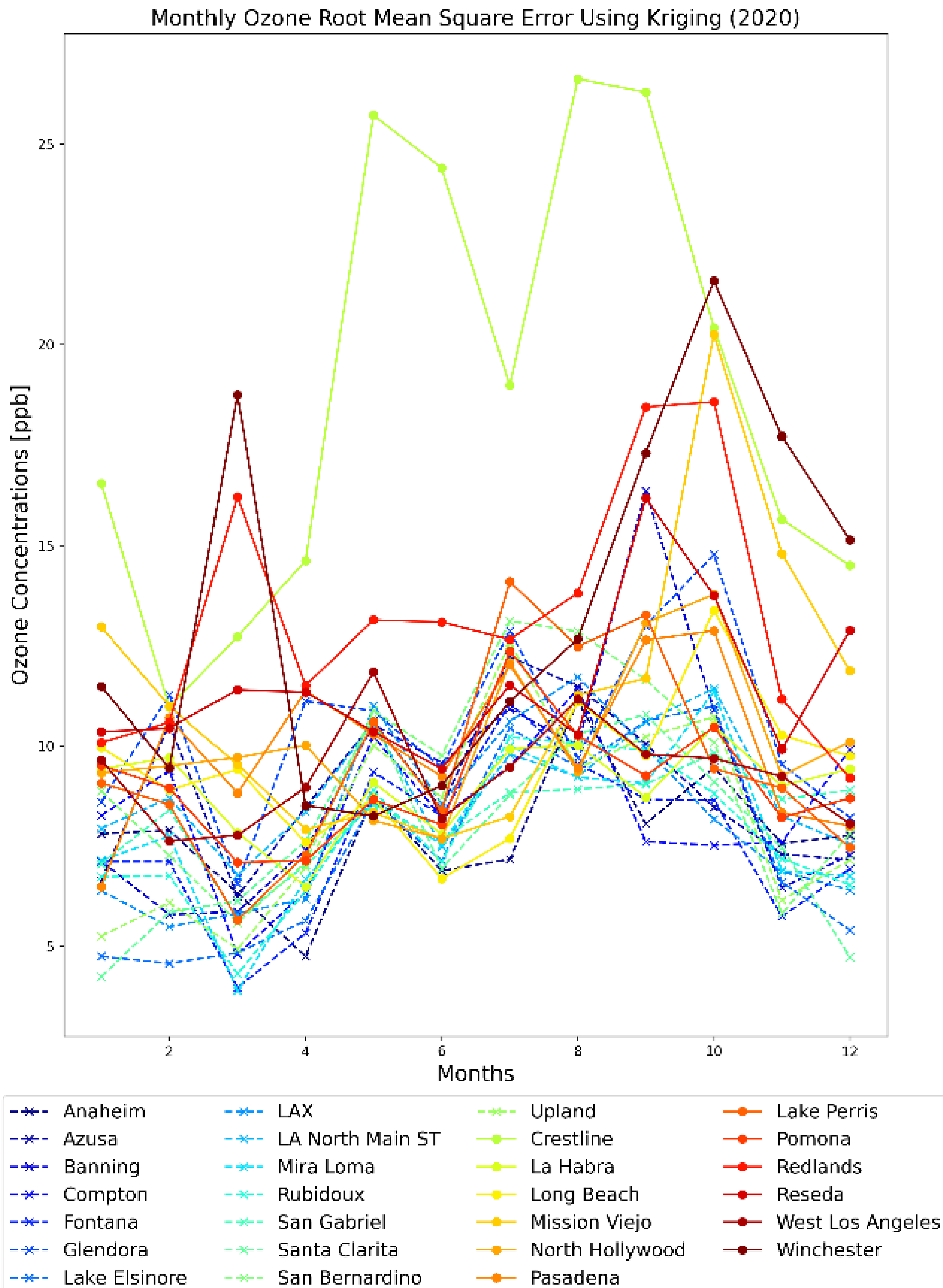


*Figure S6. Monthly ozone mean bias from spatial interpolation for 2020 using the Kriging method. The dash lines with x-markers are fifteen building sites, and solid lines with filled dots are the evaluation sites.*

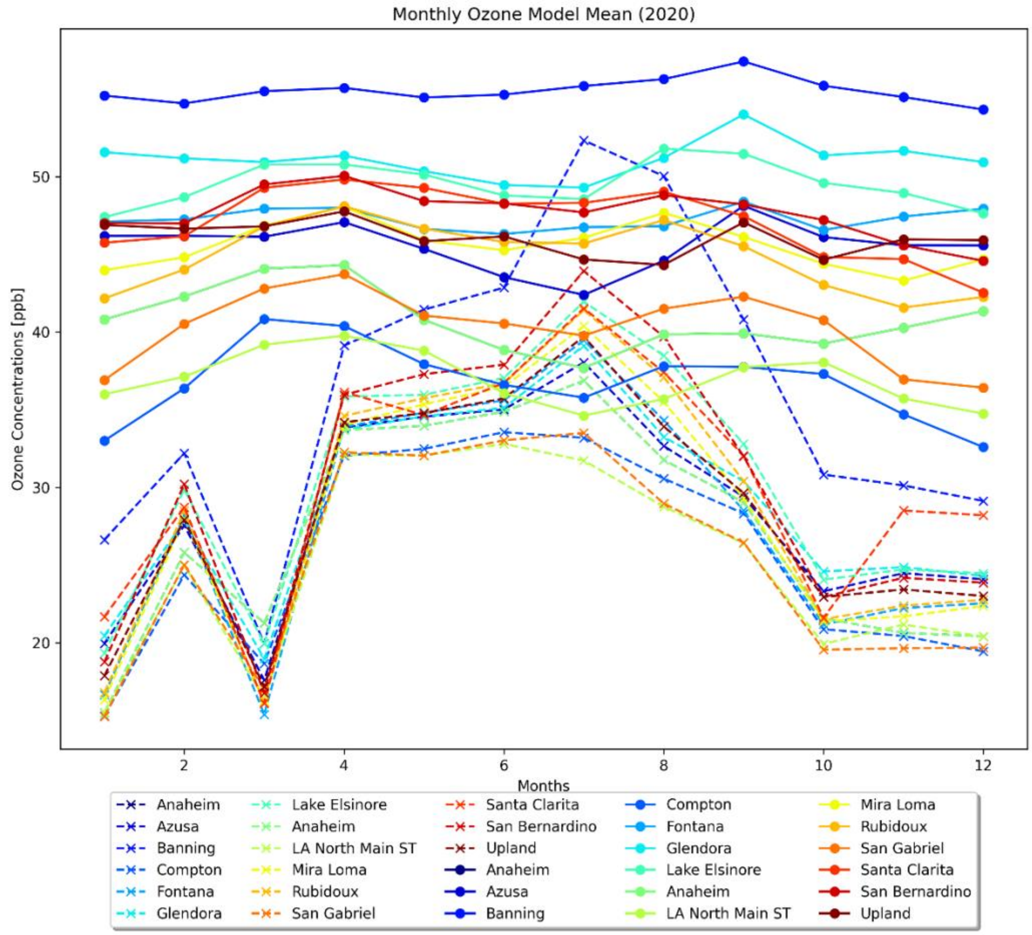


*Figure S7. CMAQ (solid lines) vs. ML building sites (dash lines) model mean.*

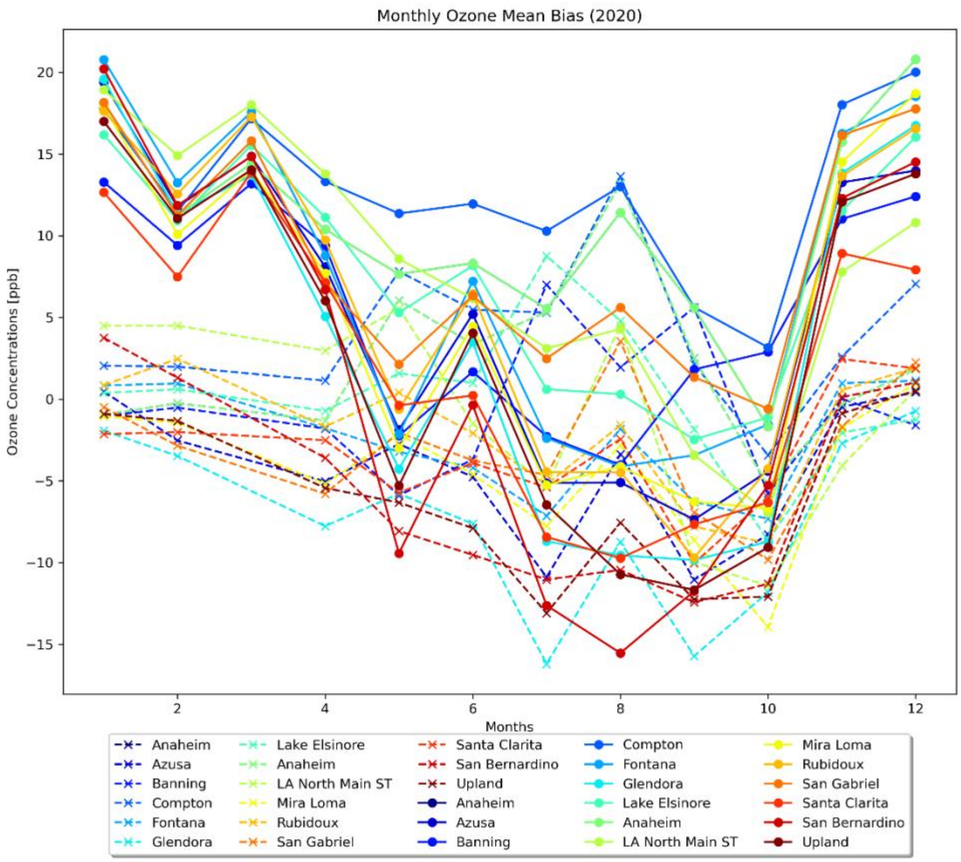


*Figure S8. Monthly mean bias computed for 2020 from 9AM to 4PM. Monthly mean bias for 15 sites using kriging interpolation method (dash lines), and CMAQ simulation (solid lines). The colors of the lines corresponded to the evaluation locations.*

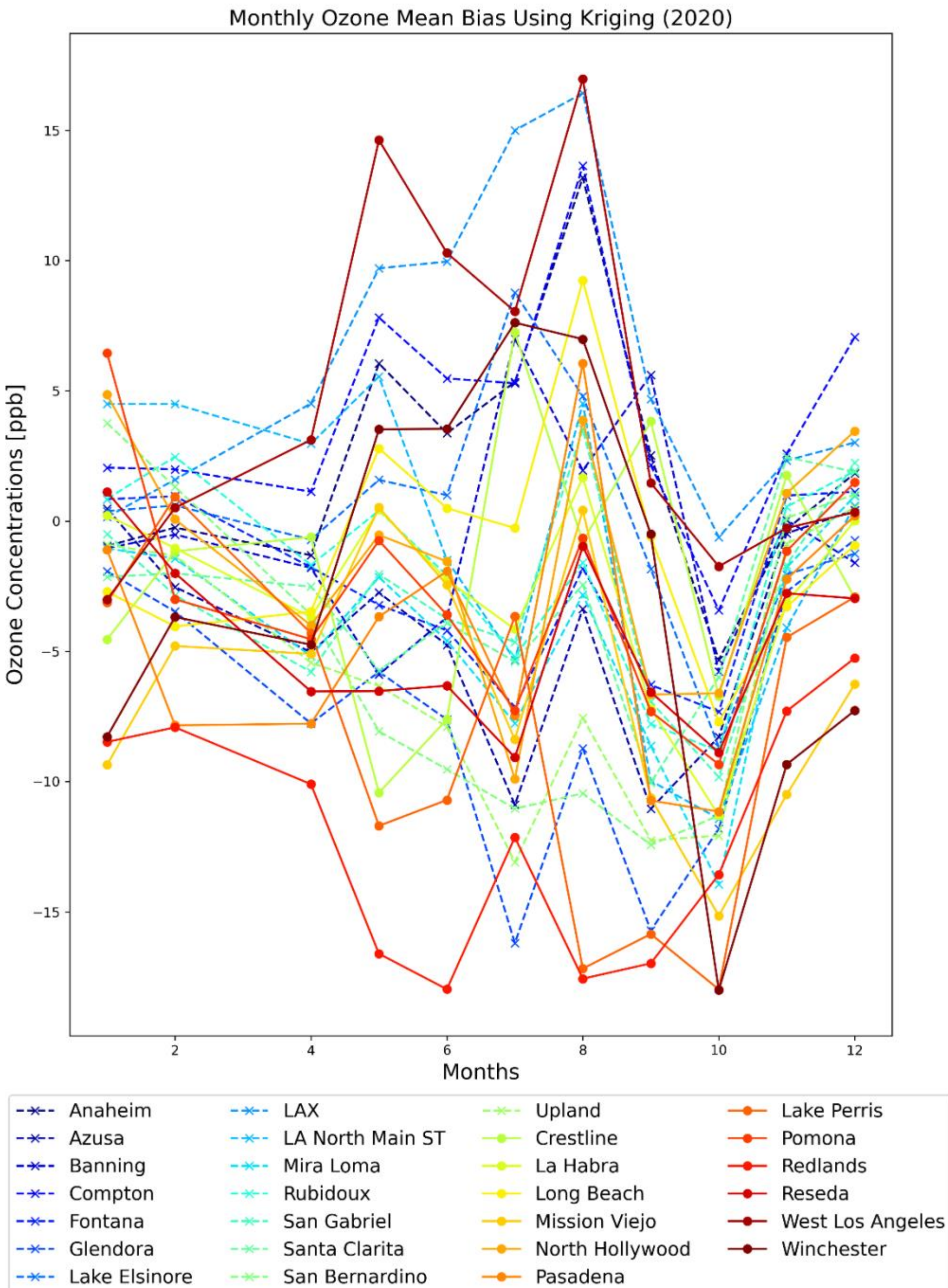


*Figure S9. Monthly ozone mean bias from spatial interpolation for 2020 using the Kriging method calculated from 9AM to 4PM. The dash lines with x-markers are fifteen building sites, and solid lines with filled dots are the evaluation sites.*

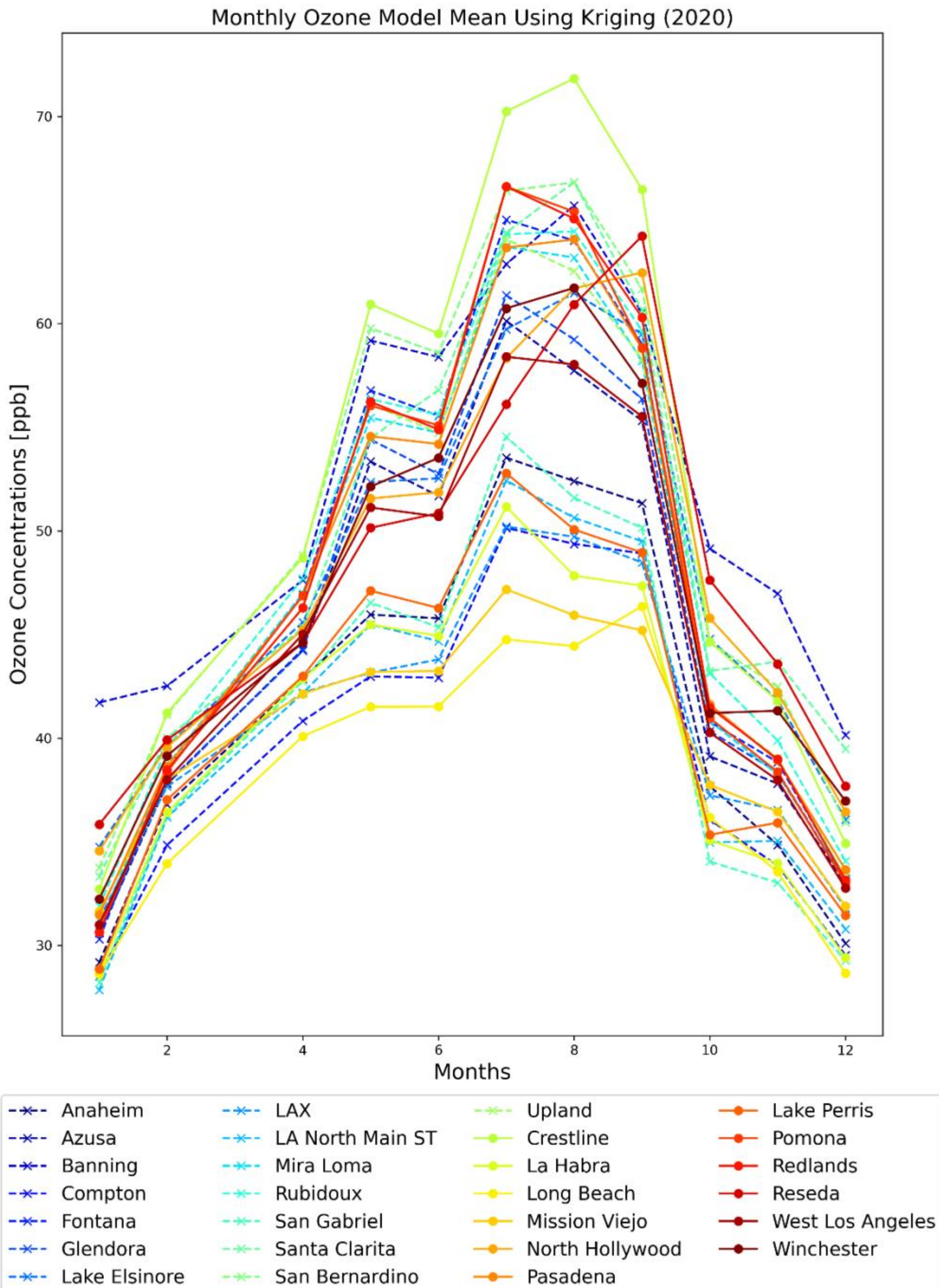


*Figure S10. Building sites vs interpolated sites from 9AM to 4PM*

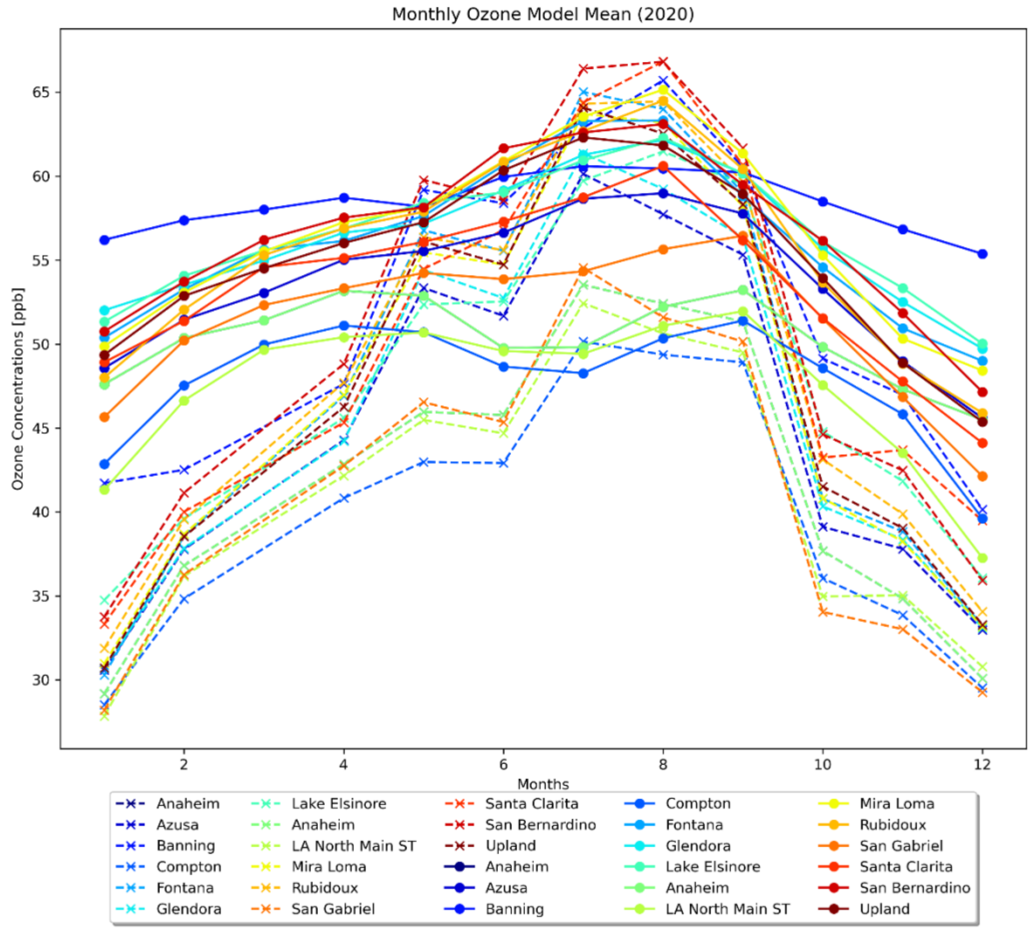


*Figure S11. CMAQ (solid lines) vs. ML building sites (dash lines) from 9AM to 4Pm.*

*Table S3. The monthly correlation coefficient for fifteen building sites using the Kriging method.*

| | Jan | Feb | Mar | Apr | May | Jun | Jul | Aug | Sep | Oct | Nov | Dec |
|---|---|---|---|---|---|---|---|---|---|---|---|---|
| **Anaheim** | 0.85 | 0.91 | 0.90 | 0.91 | 0.71 | 0.81 | 0.89 | 0.86 | 0.88 | 0.87 | 0.89 | 0.86 |
| **Azusa** | 0.80 | 0.66 | 0.96 | 0.89 | 0.85 | 0.91 | 0.93 | 0.91 | 0.95 | 0.90 | 0.86 | 0.75 |
| **Banning** | 0.89 | 0.87 | 0.94 | 0.81 | 0.86 | 0.88 | 0.80 | 0.84 | 0.66 | 0.86 | 0.92 | 0.87 |
| **Compton** | 0.87 | 0.91 | 0.92 | 0.90 | 0.77 | 0.80 | 0.91 | 0.86 | 0.88 | 0.89 | 0.90 | 0.88 |
| **Fontana** | 0.86 | 0.88 | 0.98 | 0.95 | 0.93 | 0.94 | 0.92 | 0.95 | 0.96 | 0.91 | 0.94 | 0.88 |
| **Glendora** | 0.75 | 0.63 | 0.95 | 0.81 | 0.85 | 0.89 | 0.87 | 0.91 | 0.92 | 0.76 | 0.81 | 0.70 |
| **Elsinore** | 0.93 | 0.94 | 0.96 | 0.89 | 0.83 | 0.90 | 0.91 | 0.91 | 0.87 | 0.89 | 0.93 | 0.92 |
| **LA** | 0.87 | 0.90 | 0.93 | 0.89 | 0.84 | 0.87 | 0.96 | 0.92 | 0.92 | 0.87 | 0.90 | 0.89 |
| **LAX** | 0.90 | 0.92 | 0.89 | 0.86 | 0.58 | 0.70 | 0.86 | 0.79 | 0.75 | 0.83 | 0.89 | 0.87 |
| **Mira Loma** | 0.90 | 0.90 | 0.98 | 0.95 | 0.91 | 0.93 | 0.92 | 0.93 | 0.95 | 0.91 | 0.93 | 0.90 |
| **Rubidoux** | 0.90 | 0.92 | 0.98 | 0.94 | 0.91 | 0.93 | 0.93 | 0.94 | 0.95 | 0.94 | 0.92 | 0.90 |
| **San Bernardino** | 0.90 | 0.92 | 0.96 | 0.93 | 0.91 | 0.94 | 0.89 | 0.92 | 0.94 | 0.93 | 0.95 | 0.87 |
| **San Gabriel** | 0.86 | 0.92 | 0.94 | 0.92 | 0.85 | 0.86 | 0.93 | 0.91 | 0.92 | 0.87 | 0.88 | 0.87 |
| **Santa Clarita** | 0.95 | 0.91 | 0.95 | 0.88 | 0.89 | 0.95 | 0.94 | 0.91 | 0.92 | 0.89 | 0.89 | 0.95 |
| **Upland** | 0.93 | 0.88 | 0.97 | 0.93 | 0.91 | 0.93 | 0.90 | 0.94 | 0.96 | 0.91 | 0.93 | 0.87 |

*Table S4. The monthly correlation coefficient for twelve evaluation sites using the Kriging method.*

| | Jan | Feb | Mar | Apr | May | Jun | Jul | Aug | Sep | Oct | Nov | Dec |
|---|---|---|---|---|---|---|---|---|---|---|---|---|
| **Crestline** | 0.38 | 0.67 | 0.72 | 0.52 | 0.60 | 0.63 | 0.62 | 0.62 | 0.57 | 0.57 | 0.53 | 0.51 |
| **La Habra** | 0.85 | 0.90 | 0.86 | 0.90 | 0.82 | 0.83 | 0.91 | 0.89 | 0.91 | 0.85 | 0.88 | 0.81 |
| **Long Beach** | 0.75 | 0.84 | 0.74 | 0.74 | 0.57 | 0.71 | 0.79 | 0.75 | 0.80 | 0.75 | 0.79 | 0.73 |
| **Mission Viejo** | 0.79 | 0.74 | 0.84 | 0.79 | 0.71 | 0.76 | 0.89 | 0.84 | 0.82 | 0.63 | 0.76 | 0.69 |
| **North Hollywood** | 0.84 | 0.88 | 0.89 | 0.81 | 0.88 | 0.89 | 0.94 | 0.90 | 0.94 | 0.86 | 0.91 | 0.83 |
| **Pasadena** | 0.86 | 0.90 | 0.90 | 0.85 | 0.86 | 0.86 | 0.91 | 0.91 | 0.93 | 0.85 | 0.88 | 0.84 |
| **Lake Perris** | 0.86 | 0.88 | 0.96 | 0.91 | 0.86 | 0.92 | 0.84 | 0.90 | 0.88 | 0.91 | 0.87 | 0.89 |
| **Pomona** | 0.83 | 0.88 | 0.93 | 0.94 | 0.90 | 0.92 | 0.90 | 0.91 | 0.95 | 0.87 | 0.90 | 0.87 |
| **Redlands** | 0.77 | 0.80 | 0.89 | 0.83 | 0.90 | 0.92 | 0.86 | 0.88 | 0.83 | 0.61 | 0.82 | 0.71 |
| **Reseda** | 0.76 | 0.82 | 0.85 | 0.72 | 0.87 | 0.88 | 0.90 | 0.87 | 0.89 | 0.89 | 0.87 | 0.71 |
| **West LA** | 0.75 | 0.82 | 0.84 | 0.74 | 0.74 | 0.74 | 0.93 | 0.85 | 0.87 | 0.81 | 0.80 | 0.76 |
| **Winchester** | 0.77 | 0.71 | 0.86 | 0.73 | 0.79 | 0.78 | 0.75 | 0.69 | 0.58 | 0.56 | 0.70 | 0.71 |

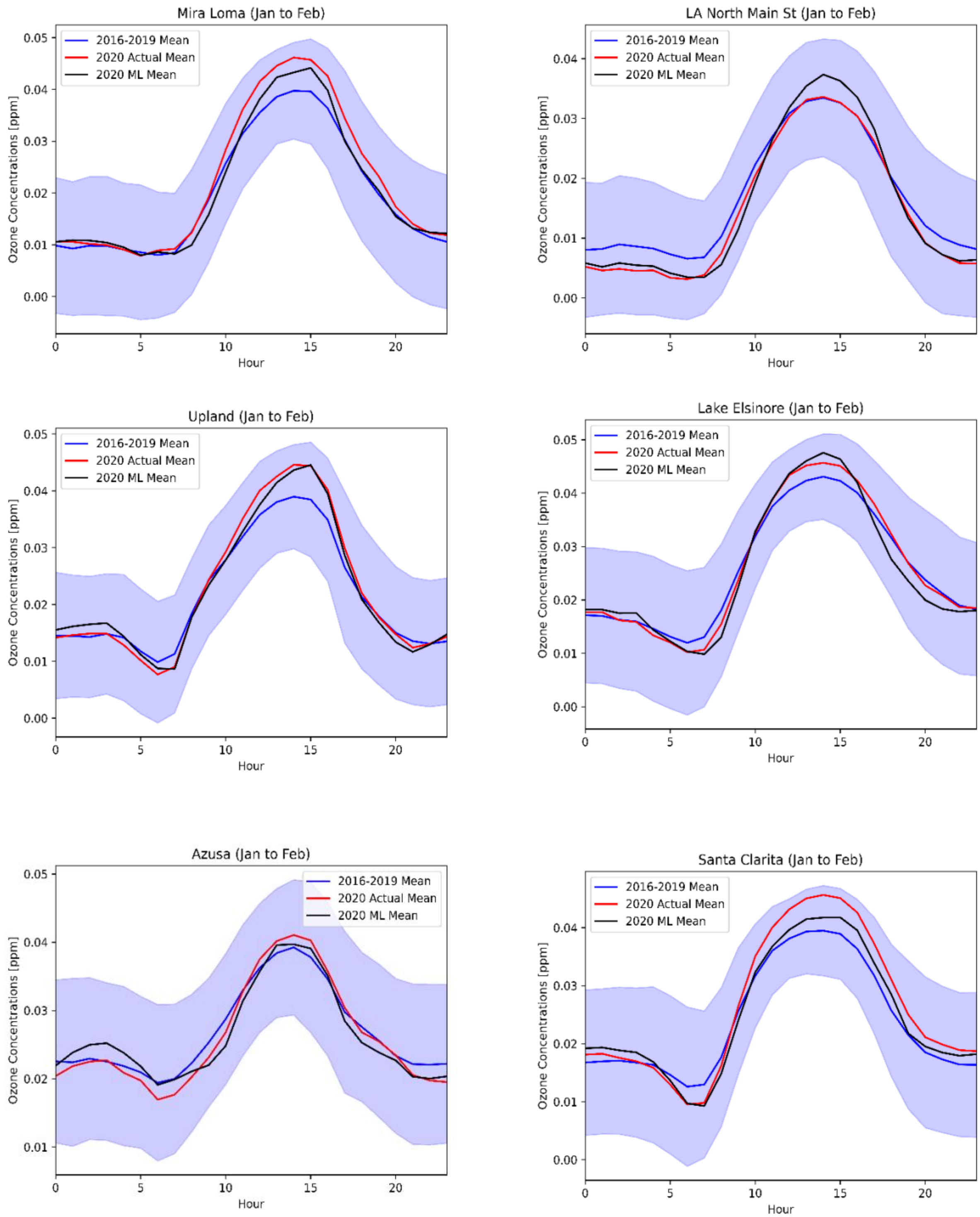

Mira Loma (Jan to Feb)
LA North Main St (Jan to Feb)
Upland (Jan to Feb)
Lake Elsinore (Jan to Feb)
Azusa (Jan to Feb)
Santa Clarita (Jan to Feb)
2016-2019 Mean
2020 Actual Mean
2020 ML Mean
Ozone Concentrations [ppm]
Hour
0.00
0.01
0.02
0.03
0.04
0.05
0
5
10
15
20

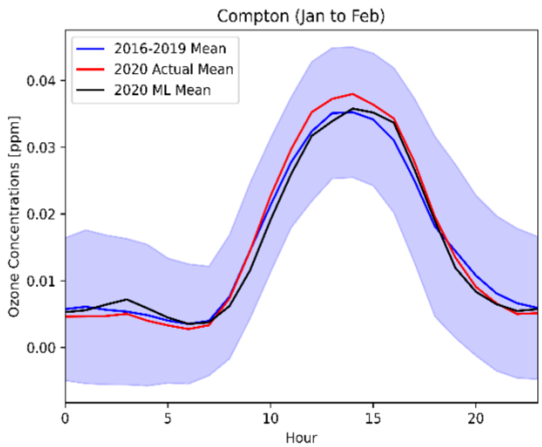
Compton (Jan to Feb)
2016-2019 Mean
2020 Actual Mean
2020 ML Mean
Ozone Concentrations [ppm]
Hour

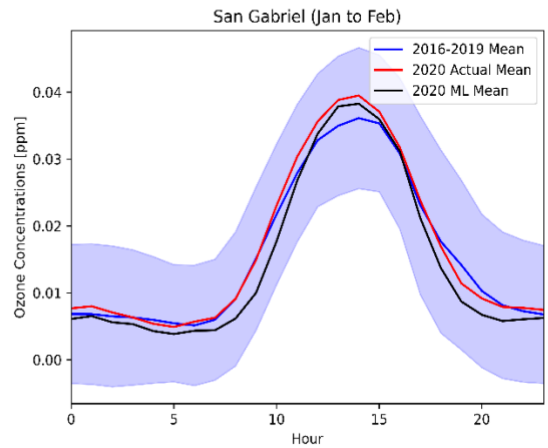
San Gabriel (Jan to Feb)
2016-2019 Mean
2020 Actual Mean
2020 ML Mean
Ozone Concentrations [ppm]
Hour

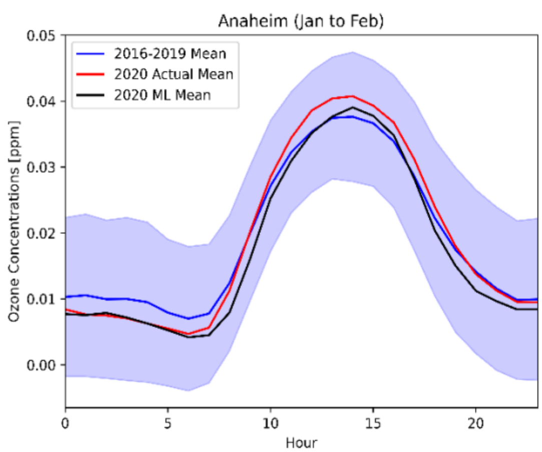
Anaheim (Jan to Feb)
2016-2019 Mean
2020 Actual Mean
2020 ML Mean
Ozone Concentrations [ppm]
Hour

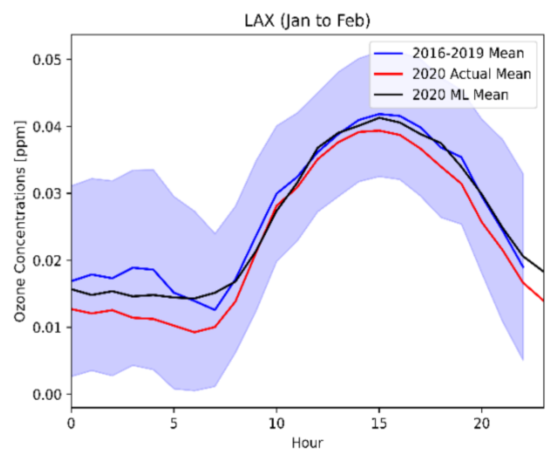
LAX (Jan to Feb)
2016-2019 Mean
2020 Actual Mean
2020 ML Mean
Ozone Concentrations [ppm]
Hour

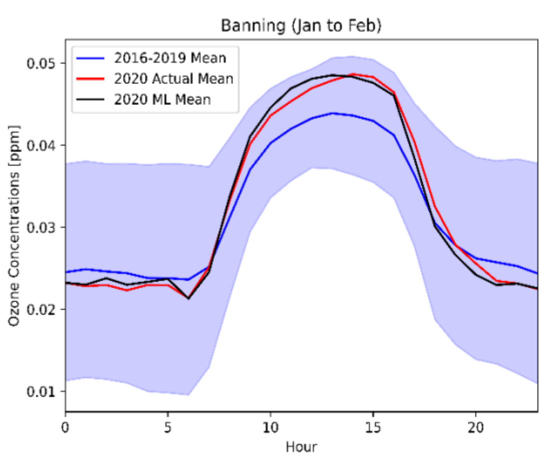
Banning (Jan to Feb)
2016-2019 Mean
2020 Actual Mean
2020 ML Mean
Ozone Concentrations [ppm]
Hour

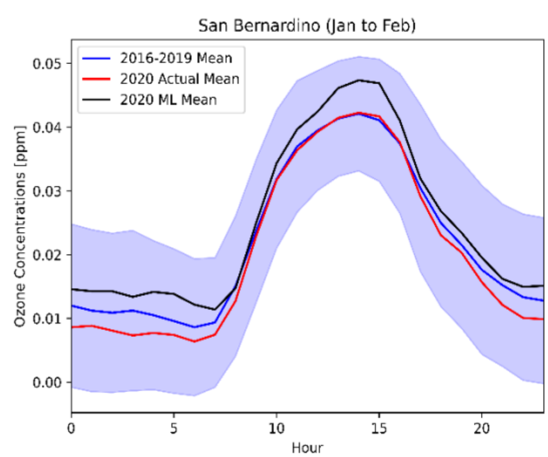
San Bernardino (Jan to Feb)
2016-2019 Mean
2020 Actual Mean
2020 ML Mean
Ozone Concentrations [ppm]
Hour

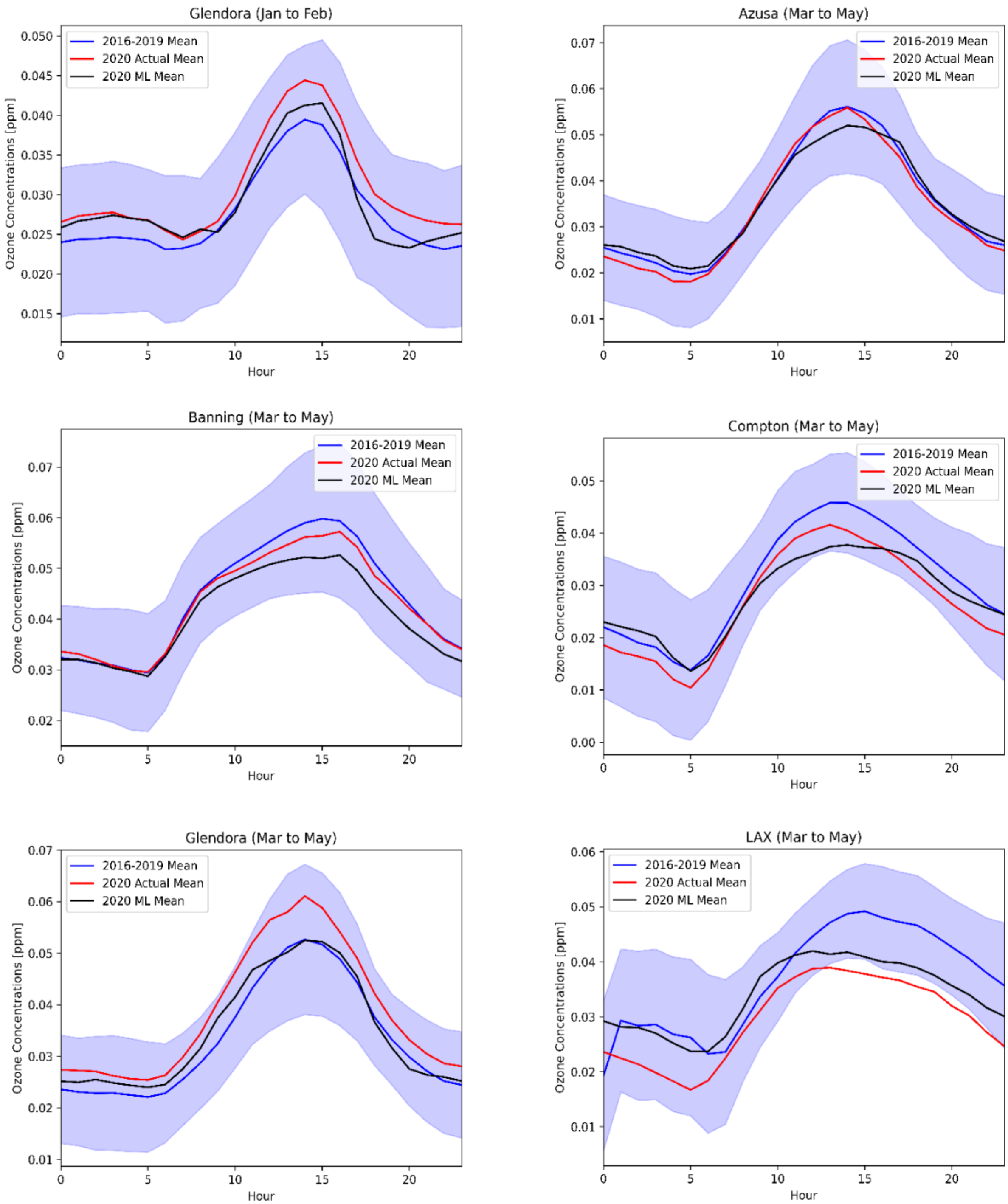

Glendora (Jan to Feb)
Azusa (Mar to May)
Banning (Mar to May)
Compton (Mar to May)
Glendora (Mar to May)
LAX (Mar to May)
2016-2019 Mean
2020 Actual Mean
2020 ML Mean
Ozone Concentrations [ppm]
Hour

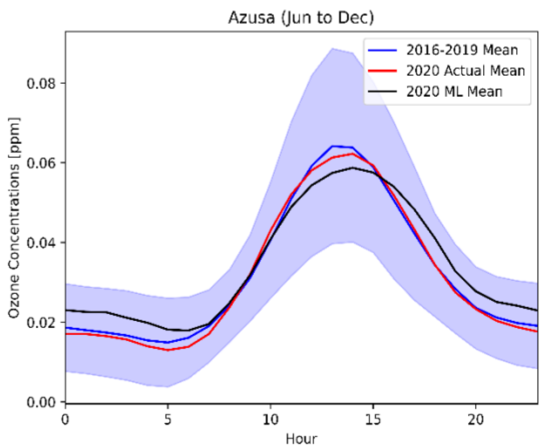
Azusa (Jun to Dec)
2016-2019 Mean
2020 Actual Mean
2020 ML Mean
Ozone Concentrations [ppm]
Hour

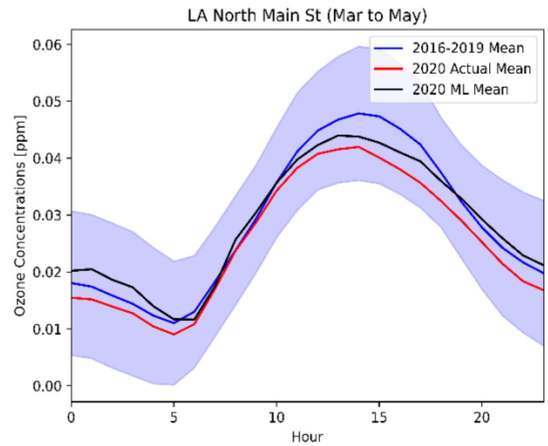
LA North Main St (Mar to May)
2016-2019 Mean
2020 Actual Mean
2020 ML Mean
Ozone Concentrations [ppm]
Hour

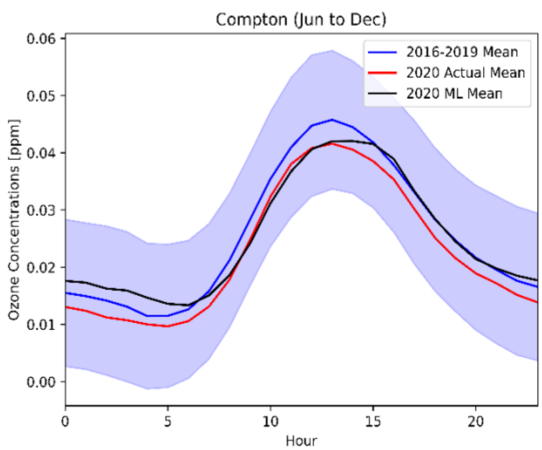
Compton (Jun to Dec)
2016-2019 Mean
2020 Actual Mean
2020 ML Mean
Ozone Concentrations [ppm]
Hour

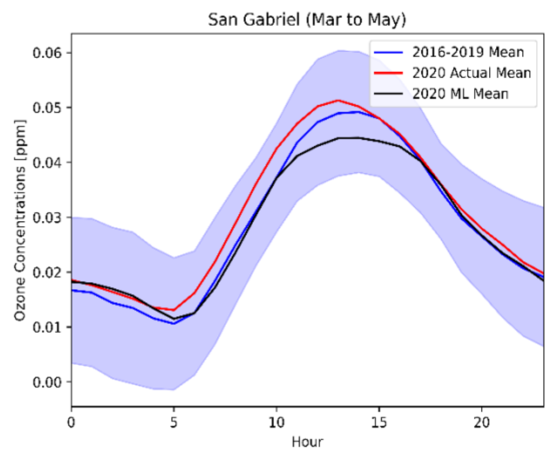
San Gabriel (Mar to May)
2016-2019 Mean
2020 Actual Mean
2020 ML Mean
Ozone Concentrations [ppm]
Hour

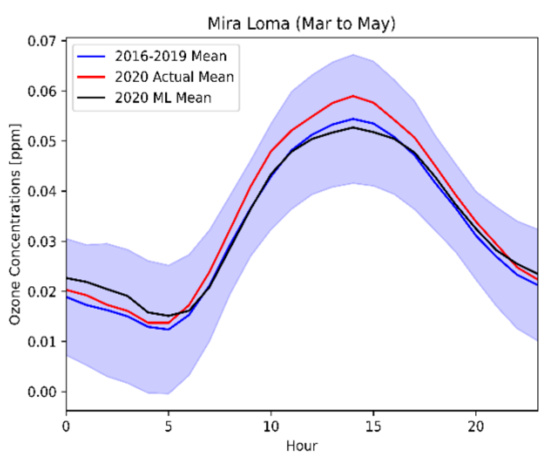
Mira Loma (Mar to May)
2016-2019 Mean
2020 Actual Mean
2020 ML Mean
Ozone Concentrations [ppm]
Hour

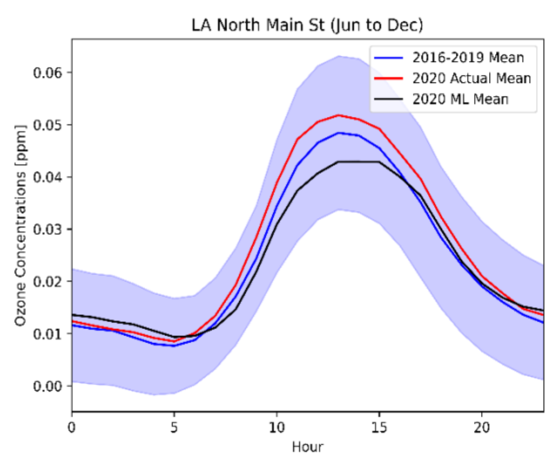
LA North Main St (Jun to Dec)
2016-2019 Mean
2020 Actual Mean
2020 ML Mean
Ozone Concentrations [ppm]
Hour

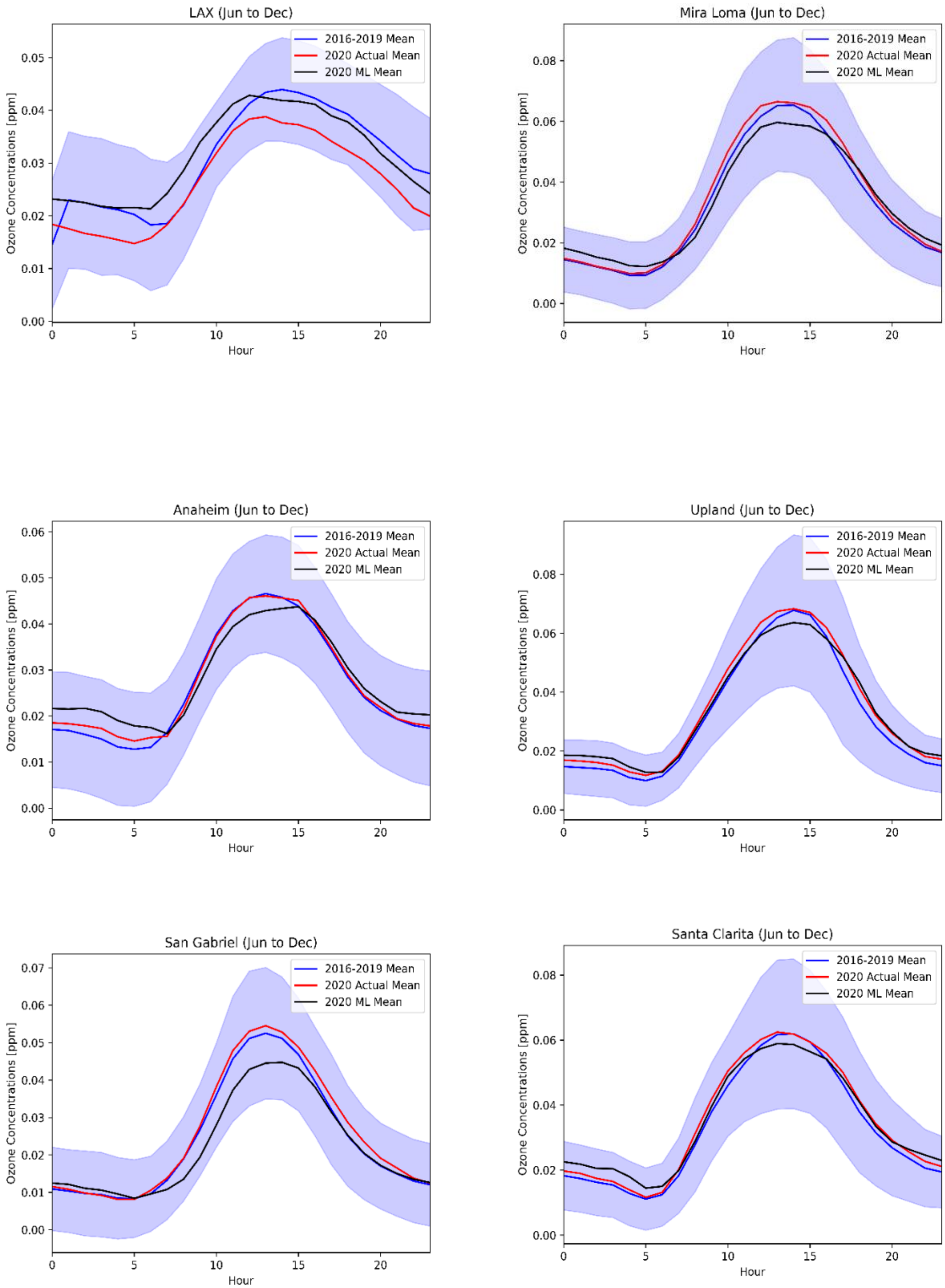
LAX (Jun to Dec)
Mira Loma (Jun to Dec)
Anaheim (Jun to Dec)
Upland (Jun to Dec)
San Gabriel (Jun to Dec)
Santa Clarita (Jun to Dec)
2016-2019 Mean
2020 Actual Mean
2020 ML Mean
Ozone Concentrations [ppm]
Hour

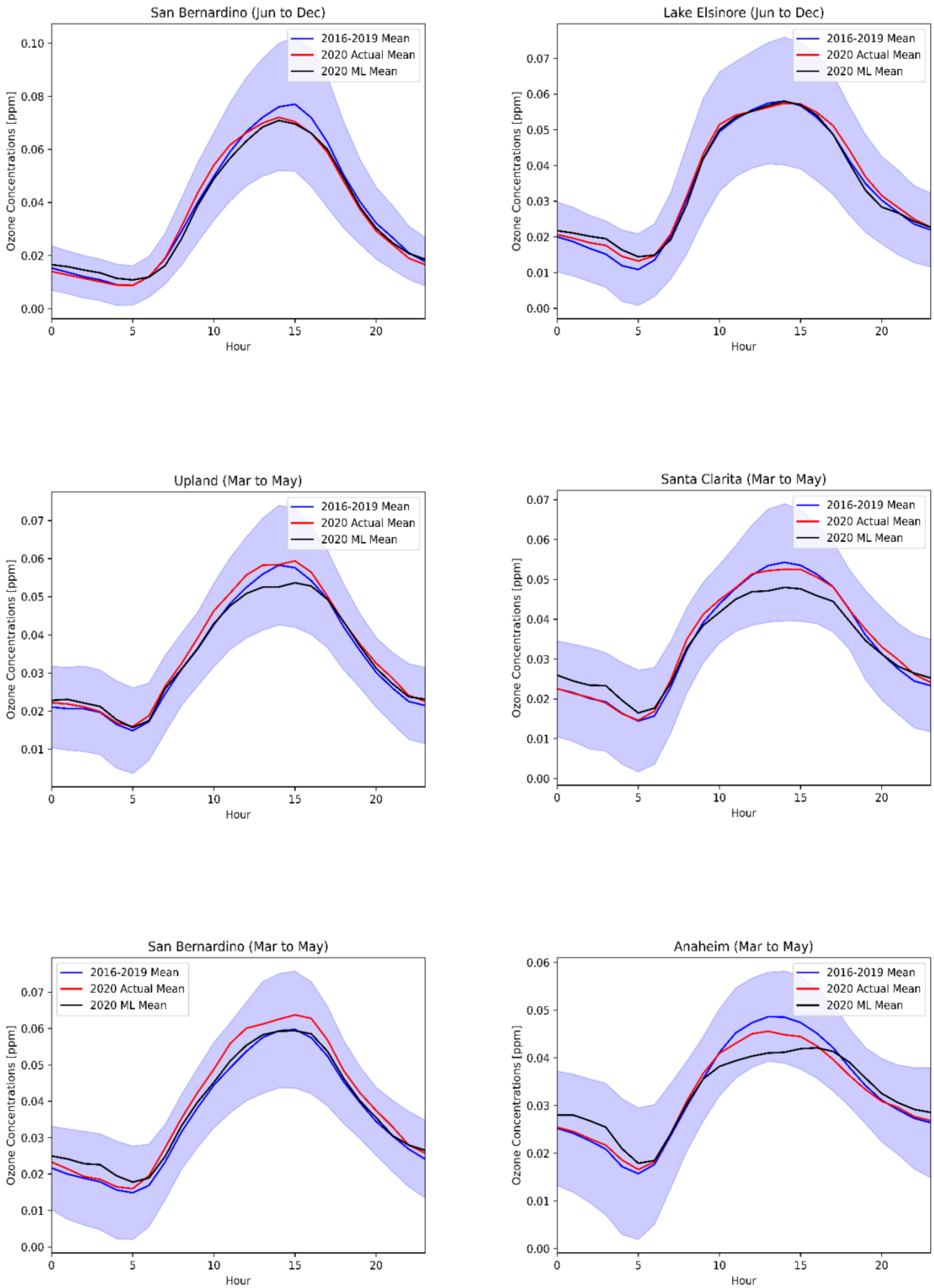
San Bernardino (Jun to Dec)
Lake Elsinore (Jun to Dec)
Upland (Mar to May)
Santa Clarita (Mar to May)
San Bernardino (Mar to May)
Anaheim (Mar to May)
2016-2019 Mean
2020 Actual Mean
2020 ML Mean
Ozone Concentrations [ppm]
Hour

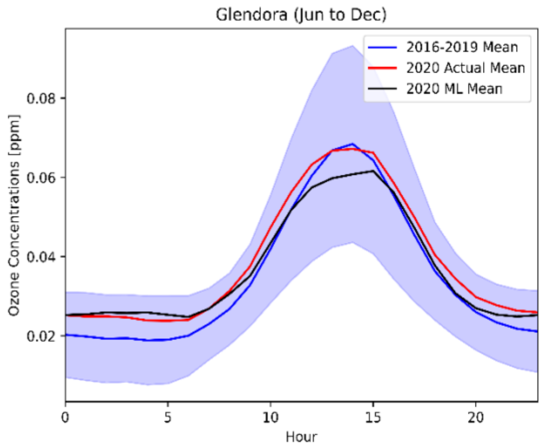


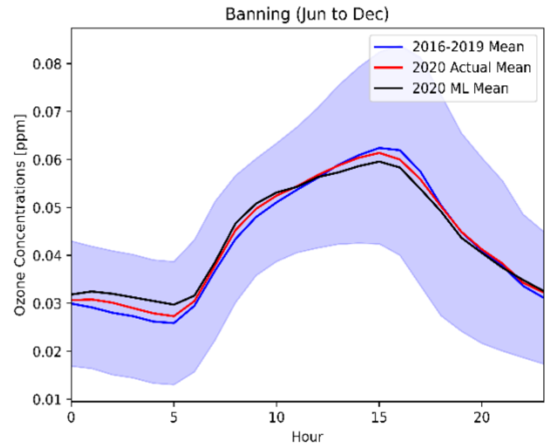


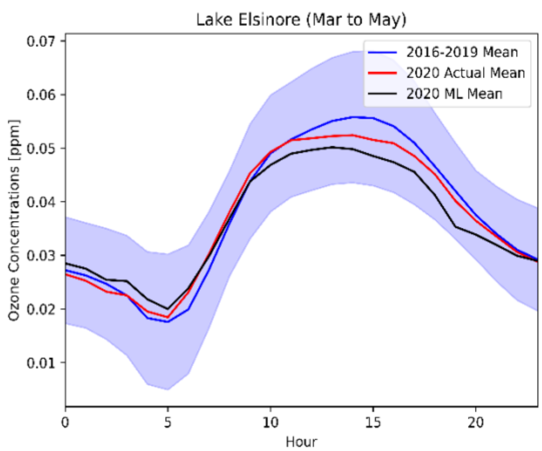


*Figure S12. Averaged diurnal profiles of 2016 - 2019 (blue), actual 2020 (red), and ML predicted 2020 (black) ozone concentrations (ppm) for three different periods, the pre lockdown (Jan to Feb), the lockdown (Mar to May), and the post lockdown period (after May). The shaded area is the standard deviation of the 2016 - 2019 measurements.*